

THE ZURICH ENVIRONMENTAL STUDY (ZENS)
OF GALAXIES IN GROUPS ALONG THE COSMIC WEB. III.
GALAXY PHOTOMETRIC MEASUREMENTS AND THE SPATIALLY-RESOLVED COLOR PROPERTIES
OF EARLY- AND LATE-TYPE SATELLITES IN DIVERSE ENVIRONMENTS [†]

A. CIBINEL,^{1*} C. M. CAROLLO^{1*}, S. J. LILLY¹, S. BONOLI², F. MINIATI¹, A. PIPINO¹, J. D. SILVERMAN³, J. H. VAN GORKOM⁴, E. CAMERON¹, A. FINOGUENOV⁵, P. NORBERG⁶, C. S. RUDICK¹, T. LU¹, Y. PENG¹

SUBMITTED TO APJ

ABSTRACT

We present photometric measurements for the 769 galaxies in the first-epoch data of the *Zurich Environmental Study (ZENS)* introduced in Carollo et al. (2012; Paper I). The main thrust of ZENS is to use a single galaxy sample to study the dependence of galaxy properties at $z \sim 0$ on the mass of the host group M_{GROUP} , the group-centric distance R (in units of the group characteristic radius R_{200}), and the large-scale structure over density δ_{LSS} . For the galaxies and, where possible, separately for their bulge and disk components, the photometric measurements consist of resolved $(B-I)$ colors, color gradients, color dispersions, and color maps, as well as stellar masses and star-formation rates, derived with the help of ancillary archival optical spectra and NUV-to-NIR photometry. We classify ZENS galaxies into three spectral types of quiescent, moderately star-forming, and strongly star-forming systems using a combination of spectral features and broad-band NUV-optical colors. This optimally distinguishes red, quiescent systems from dust-reddened star-forming galaxies, which contribute up to 50% to the $(B-I)$ “red sequence” at $\sim 10^{10} M_{\odot}$. Our photometric database is made available for public use in the global ZENS catalog published in Paper I, and will be used in future ZENS analyses dedicated to assessing the impact of different environments on the stellar populations and star formation properties of galaxies. In this paper, we study, at fixed stellar mass and Hubble type, how $(B-I)$ colors, color gradients and color dispersion of *bulge-dominated and disk-dominated satellites* depend on M_{GROUP} , R/R_{200} and δ_{LSS} . We find that the large-scale structure density field does not have a strong impact on either the colors, the color gradients or the color scatter of either disk- or bulge-dominated satellites. Indeed, bulge-dominated satellites are rather insensitive to any environmental parameter. The strongest environmental effects are found for disk-dominated satellites with group-centric distance. At constant galaxy mass, these satellites are redder in the cores compared with the outskirts of groups; at galaxy stellar masses $> \sim 10^{10} M_{\odot}$, they also have shallower $(B-I)$ color gradients within $0.6R_{200}$ than at larger group-centric distances. Our results support a picture where galaxies undergo a relatively fast quenching of their star formation in their outer disks on timescales $\tau_{quench} \lesssim 2$ Gyr, as they progressively move deeper inside the potentials of their host groups.

Subject headings: surveys - galaxies: groups - galaxies: photometry - galaxies: evolution

1. INTRODUCTION

The history of the growth of stellar mass in the Universe is imprinted in the properties of star forming and quiescent (passively-evolving) galaxy populations at different epochs, and, at each epoch, in different environments. In the local Universe, where large surveys such as the 2dFGRS (Colless et al. 2001) and the SDSS (York

et al. 2000) have made possible the comparison of statistically complete, large samples of galaxies (e.g. Brinchmann et al. 2004; Tremonti et al. 2004; Baldry et al. 2006; van der Wel 2008; Peng et al. 2010), and, to some extent, also at higher redshifts (e.g., Daddi et al. 2007; Noeske et al. 2007; Salim et al. 2007; Pannella et al. 2009; Karim et al. 2011), star formation rates (and other properties such as nuclear activity, gas content, metallicity and structure) have been shown to strongly depend on galaxy stellar mass. It has also been established that galaxies with high star formation rates are rarer in dense environments, and that galaxy groups and clusters host a much higher fraction of quiescent, gas poor, early-type galaxies, relative to the field (e.g. Oemler 1974; Dressler 1980; Balogh et al. 2004; Croton et al. 2005). These results have clearly indicated an effect of the environment on the production of new stars in galaxies. Given however that there is some evidence that galaxy mass function varies with local environmental density (Baldry et al. 2006; Bundy et al. 2006; Bolzonella et al. 2010; Kovač et al. 2010), the environmental effects need to be carefully disentangled from those of galaxy mass. Analyses of

* E-mail: cibinel@phys.ethz.ch, marcella@phys.ethz.ch

¹ Institute of Astronomy, ETH Zurich, CH-8093 Zurich, Switzerland

² Institute for Theoretical Physics, University of Zürich, Winterthurerstrasse 190, CH-9057 Zürich, Switzerland

³ Institute for the Physics and Mathematics of the Universe (IPMU), University of Tokyo, Kashiwa-shi, Chiba 277-8568, Japan

⁴ Department of Astronomy, Columbia University, New York, NY 10027, USA

⁵ Max-Planck-Institut für extraterrestrische Physik, D-84571 Garching, Germany

⁶ Institute for Computational Cosmology, Department of Physics, Durham University, South Road, Durham DH1 3LE, UK

[†] Based on observations collected at the European Southern Observatory, La Silla Chile. Program ID 177.A-0680

the SDSS have shown that, over about two dex of galaxy mass, the fraction of red galaxies rises with increasing environmental density (Baldry et al. 2006; Bamford et al. 2009).

Recently, Peng et al. (2010) have presented a phenomenological approach to galaxy evolution that is constructed around the basic continuity equation for galaxies, coupled with a small number of observationally derived axioms, which are based on a handful of striking simplicities exhibited by the galaxy population. In their analysis those authors show that the “quenching” transition of galaxies from the blue cloud to the red sequence is due to a fully-separable combination of two processes, one dependent on the stellar mass of a galaxy (or a proxy), independent of the environment, and the other dependent on the environment, independent of the galaxy stellar mass. The former “mass-quenching” process has a rate proportional to the star-formation rate and it is this process that controls the mass functions of both active and passive galaxies. In Peng et al. (2010, 2012) the differences in the overall mass functions arise primarily through the secondary effect of merging of post-quenching passive galaxies.

A key open question at this point is which of the many characteristics of a given galaxy’s environment most strongly affects its ability to form new stars. For instance, the environment of a galaxy can be described by the mass of the host group/cluster halo in which the galaxy resides, its precise location (the distance from the group/cluster center) or its rank within it as a central or satellite galaxy, or by the underlying density field that is produced by the cosmic large-scale filamentary structure (LSS).

There is theoretical support for practically all these different aspects of “environment” to be in principle important. A number of studies have postulated the existence of a typical halo mass scale, of about $10^{12}M_{\odot}$, above which the interplay between shock heating and feedback from, e.g., AGNs, makes the cooling of the intergalactic medium and subsequent star-formation progressively inefficient (e.g. Dekel & Birnboim 2006; Cattaneo et al. 2006; Khochfar & Ostriker 2008). An environmental dependence of the halo assembly histories could also be at the origin of the relation between galaxy star formation activity (and morphology) and environment (e.g., Sheth & Tormen 2004; Gao et al. 2005; Maulbetsch et al. 2007; Hahn et al. 2007, 2009; Crain et al. 2009). This makes it imperative that observational studies distinguish between these different aspects of the environment of a galaxy.

A further plausible explanation within a CDM framework is that star-formation is suppressed in galaxies once these are accreted into bigger haloes, where they may suffer from ram pressure stripping of their cold gas (Gunn & Gott 1972) or removal of their hot gas (Larson et al. 1980; Balogh et al. 2000). Peng et al. (2012) find that their environment-quenching in the general galaxy population is confined to processes acting on the satellite population (“satellite-quenching”), with a fraction of satellite galaxies which experience such quenching ranging from 30% to 75%, depending on the local density, but not at all on halo mass (above $10^{12}M_{\odot}$). Environmental effects may thus be relevant as galaxies enter group-sized halo potentials and there become satellites of the central galaxy.

The precise mass scale at which “halo” physics may start influencing the star formation properties of satellite galaxies is also not well known. There are indications that galaxy properties start showing signatures of environmental effects at the mass scales typical of galaxy groups. For example, numerical simulations show that galaxies are depleted of their cold and hot gas as they enter the virialized regions of groups (e.g., Kawata & Mulchaey 2008; Feldmann et al. 2011). Furthermore, analyses of SDSS groups have shown that, at fixed stellar mass, satellites in groups are on average redder than central galaxies (van den Bosch et al. 2008; Skibba 2009; Weinmann et al. 2009). Galaxies may thus be quenched as they become satellites in groups, before these assemble into larger cluster-sized structures. On the other hand, Peng et al. (2012) have argued that many of the key evolutionary processes on satellites, namely the specific star-formation rates (sSFR) of star-forming galaxies, the mass-quenching process and the environment-quenching (at fixed density) are all strikingly independent of halo mass, above $10^{12}M_{\odot}$. Furthermore, the correlation with halo mass of the red fraction at fixed stellar mass cited above can be explained, at least qualitatively, in terms of the subsequent increase in halo mass, without an increase in stellar mass, for quenched objects.

Given the many possible ways to transform star forming galaxies into red-and-dead stellar systems, the challenge is to eliminate possibilities. New constraints are needed, as these have been typically limited to integrated galaxy properties (e.g., total galaxy colors and star formation rates), and have provided little knowledge on whether and to what extent the environmental forcing affects the bulge or disk components of galaxies, or both. Also, morphological analyses of the satellite and central galaxy populations have been typically based on a separation into early- and late-type galaxies by means of a threshold in either galaxy concentration or Sérsic index n (Sersic 1968), which leads to mixing of galaxies with very different bulge-to-disk ratios, arguably the most physical diagnostics to classify galaxy structure and morphology (see Cibinel et al. 2012a, hereafter Paper II). The question thus remains whether the strength of environmental effects varies between galaxy populations with different bulge-to-disk ratios.

To make headway in understanding the physical origin of the environmental dependence of galaxy properties, we have undertaken the *Zurich Environmental Study* (ZENS, Carollo et al. 2012a, hereafter Paper I), a comprehensive study of detailed galaxy properties as a function of group halo mass, projected group-centric distance, large-scale structure (LSS) density, and central/satellite ranking within the group potentials. ZENS uses the same local galaxy sample to perform the environment-vs-environment comparisons, which eliminates any bias when interpreting the results. Detailed structural properties for the ZENS galaxies and their bar, bulge and disk components have been presented in Paper II, which enable us to investigate important questions such as those highlighted above.

In several follow-up papers we will investigate the detailed properties of galaxies in the different environments explored in ZENS (e.g., Lu et al. (2012), Paper IV, where we study the fraction of passive satellite galaxies of differ-

ent morphologies; Rudick et al. (2012), Paper V, where we analyze the integrated colors of the disk and bulge components of both central and satellite galaxies; Pipino et al. (2012), Paper VI, where we compare the star formation properties of merging central and satellite galaxies with non-interacting galaxies of similar stellar masses.

In this third paper in the ZENS sequence we present the methodology adopted to measure the photometric properties of ZENS galaxies, and the tests that we have performed to assess the impact of systematic errors on these properties. The photometric measurements include galaxy star formation rates, stellar masses, colors, color gradients, two-dimensional color maps, as well as e.g., bulge/disk colors and masses, etc. Furthermore, as a first utilization of these photometric measurements, and using also the structural measurements for the ZENS galaxies presented in Paper II and the environments characterized in Paper I, we discuss the $(B - I)$ colors and color gradients of *satellite* galaxies as a function of galaxy mass at constant Hubble type, and of group halo mass, group-centric distance and LSS density.

This paper is structured as follows. We briefly summarize ZENS in Section 2. The first part of the paper is dedicated to the description of the photometric analyses performed on the ZENS galaxy sample: Stellar masses, both for the entire galaxies and their bulge and disk components, and mass completeness limits are derived using synthetic templates and broad-band photometry in Sections 3-4. Section 5 presents the criteria that we have used to classify strongly and moderately star-forming galaxies, and quiescent galaxies, based on the combination of spectral features and far- and near-UV (FUV/NUV) versus optical colors, as well as fits to the galaxy Spectral Energy Distributions (SEDs). We also highlight in this Section the importance of the comparison of multiple star formation diagnostics, to avoid misclassifications due to, e.g., spectra targeting only the quiescent bulges of star forming disks, individual colors appearing red due not to quiescent stellar populations but rather to dust in star forming systems. We discuss the derivation and associated systematic biases of resolved color maps and radial color profiles in Section 6. Section 7 shows the dependence of colors, color gradients and color scatter at fixed stellar mass for the different Hubble types determined in Paper II. The final Section 8 presents our first environmental study of the presented measurements, i.e., the dependence of colors, color gradients and color scatter in *disk satellites* on the different environmental parameters. We summarize the paper in Section 9. In Appendix A we provide supplementary information on the tests we performed to assess the reliability of galaxy properties derived from our SED fits. Throughout the paper we will assume the following values for the relevant cosmological parameters: $\Omega_m = 0.3$, $\Omega_\Lambda = 0.7$ and $h = 0.7$. Magnitudes are in the AB-system (Oke 1974).

The photometric measurements for the ZENS galaxies that we present in this paper are published electronically in the ZENS catalog associated with Paper I.

2. A SUMMARY OF ZENS

The *Zurich Environmental Study* uses 141 groups of galaxies selected from the 2dFGRS Percolation-Inferred Galaxy Group (2PIGG) catalogue (Eke et al. 2004). The

groups were randomly selected from all groups in the 2PIGG catalogue which are located at $0.05 < z < 0.0585$ and have at least 5 spectroscopically-confirmed galaxy members. New B - and I -band observations were taken with the WFI camera mounted at the MPG/ESO 2.2m Telescope, reaching a background-limited depth of $\mu(B) = 27.2$ mag arcsec $^{-2}$ and $\mu(I) = 25.5$ mag arcsec $^{-2}$ over an area of 1 arcsec 2 . We refer to Paper I for details on the ZENS sample, data reduction and calibration of the WFI data, and our environmental definitions, and to Paper II for details on the structural measurements and morphological classification of the ZENS galaxies.

Briefly, in ZENS we focus our attention on the following measures of galactic environment:

1. the mass of the group halo in which galaxies reside, M_{GROUP} ;
2. the distance of a galaxy from the center of the host group, normalized to the characteristic group radius R_{200} ;
3. the large scale (over)density field δ_{LSS} , quantified through the overdensity of 2PIGG *groups* at the ZENS field positions, within a circular projected area of size equal to the comoving distance to the 5th nearest 2PIGG group, i.e., $\delta_{LSS} = \frac{\rho_{LSS}(z) - \rho_m}{\rho_m}$ (with $\rho_{LSS}(z)$ the density of 2PIGG groups out to the 5th nearest neighboring group, and ρ_m the mean projected density in the 2dFGRS volume);
4. the rank of the galaxy within the host group, i.e., whether the galaxy is the central galaxy or a satellite galaxy in orbit around the central.

Attention was paid to ascertain whether the ranking of galaxies as centrals and satellites led to a self-consistent solution for the central galaxies (required to be the most massive, within the errors on the estimated stellar masses, as well as compatible with being the geometrical and velocity centroids of the groups). Groups with a well-identified central galaxy were defined as “relaxed”, while groups in which no galaxy member satisfied all requirements to be considered a central galaxy were defined to be “unrelaxed”.

Note that the full ZENS sample contains 1630 galaxies in 141 galaxy groups; ZENS Papers I-VI, however, including this paper (III), are based on the first-epoch dataset that contains 769 galaxies in 79 of the ZENS groups.

3. STELLAR MASSES FOR THE ZENS GALAXIES

To estimate the stellar masses (hereafter M_{galaxy} or, when unambiguous, simply M for simplicity) for the ZENS galaxies we fitted synthetic spectral templates to their broad-band photometric data. To this end we employed our code *ZEBRA+* (*The Zurich Extragalactic Bayesian Redshift Analyzer Plus*, Oesch et al. (2010)), an upgrade of the public version of the ZEBRA package presented in Feldmann et al. (2006). Relative to ZEBRA, the upgraded ZEBRA+ code enables the use of synthetic templates for the estimation of stellar masses, ages and metallicities. In the following we describe in detail the photometric data and the model templates used to derive the galaxy stellar masses.

Table 1
Fraction of ZENS galaxies with available multi-band photometry

Band	Coverage
FUV, NUV (GALEX)	85%
B, I	100%
u, g, r, i, z (SDSS)	15%
J, H, K (2MASS)	97%

Note. — The fraction of first-epoch ZENS galaxies with available photometric data from the listed surveys.

3.1. Photometry

In order to constrain at best the template fits, we combined all available photometry for the sample galaxies, including our new WFI *B* and *I* imaging data as well as data from the literature. Specifically, for each galaxy we used, when available, SDSS *u*, *g*, *r*, *i*, *z* (Abazajian et al. (2009)), 2MASS *J*, *H*, *K*, (Skrutskie et al. 2006) and GALEX NUV and FUV magnitudes. The fraction of ZENS galaxies in the first-epoch sample with observations at any given wavelength is summarized in Table 1.

We calibrated the data products from these survey following the instructions provided by the respective teams. For the SDSS we used the legacy imaging data with the “best” reduction from the Data Release 7 (DR7) and for 2MASS we use the Atlas data product. In the case of GALEX we used the GR6 All-sky Survey (AIS) tiles or, when available, the deeper Medium Survey (MIS) intensity maps. In case of more than one AIS observation, we used the data having the longer exposure time.

We measured the magnitudes in all pass-bands using an elliptical aperture equal to $2 \times R_{pMAX}$, with R_{pMAX} the larger of the two Petrosian semi-major axes R_{pI} and R_{pB} measured with SExtractor (Bertin & Arnouts 1996) on the WFI *I*- and *B*-band images. When available we used the sky-background estimates or maps provided by the survey pipelines, otherwise the background was subtracted using the mode of the intensity in the pixels located outside the Petrosian aperture. A comparison between the fluxes we measured and those found in the survey’s public catalogues is shown in Figure A1 of Appendix A, together with a discussion on possible biases arising from differences in the average PSF in the different passbands.

All the magnitudes were corrected for galactic extinction using $E(B - V)$ values from the survey catalogues, if provided, or obtained from the dust maps of Schlegel et al. (1998), assuming a Cardelli et al. (1989) extinction law. For correcting GALEX magnitudes, we applied the relations $A_{FUV}/E(B - V) = 8.376$ and $A_{NUV}/E(B - V) = 8.741$ as derived by Wyder et al. (2005). 2MASS magnitudes were converted into the AB system by applying the following transformations which we calculated using the IRAF package `synphot` and the composite Vega spectrum released by STSC⁹: $J_{AB} = J_{VEGA} + 0.894$, $H_{AB} = H_{VEGA} + 1.367$ and $K_{AB} = K_{VEGA} + 1.837$.

⁹ <http://www.stsci.edu/hst/observatory/cdbs/calspec.html>

Before calculating the masses we ran ZEBRA+ in the *photometry-check mode* in order to correct for possible systematics in the calibration of the input catalogue. With this option it is possible to detect residuals between the best-fit template and the galaxy fluxes which are independent of template type itself (see Feldmann et al. (2006) for more details). This check revealed that there was a small offset in the SDSS *i*- and *z*-bands equal to -0.03 and 0.04 magnitudes, respectively. We applied these small shifts to the SDSS *i*- and *z*-band before proceeding to the derivation of masses for our galaxies.

3.2. Synthetic template library

To model the spectral energy distribution of the ZENS galaxies we used a set of Bruzual & Charlot (2003) synthetic models with a Chabrier (Chabrier (2003)) initial mass function, truncated at $0.1M_{\odot}$ and $100M_{\odot}$ and based on the Padova 1994 evolutionary tracks. We used star formation histories (SFH) described by exponentially declining SFRs $\psi(t) = \psi_0 \tau^{-1} e^{-t/\tau}$, with different values for the characteristic time τ , as well as by a constant SFR (CSF, $\tau \rightarrow \infty$). The normalization factor ψ_0 was set to 1 by imposing a total mass of $1M_{\odot}$ at time $t \rightarrow \infty$. Each star formation history was sampled with 900 templates of metallicities Z ranging between 0.004 ($1/5Z_{\odot}$) and 0.04 ($2Z_{\odot}$) and ages between 10 Myr and 12 Gyr.

Reddening produced by dust was also taken into account: a dust correction was allowed in the ZEBRA+ fits, and often required for galaxies morphologically classified as spirals or irregular. The dust extinction was assumed to be described by a Calzetti law (Calzetti et al. 2000) and the corresponding reddening $E(B - V)$ was allowed to vary between 0 and 0.5, in 27 fine steps. A substantial dust attenuation - $E(B - V) > 0.25$ - was permitted only for star-forming templates, i.e., templates with $\text{Age}/\tau < 4$ (see also Pozzetti et al. (2007); Ilbert et al. (2010)) and for galaxies not classified as quiescent (see Section 5). Galaxies with a best-fit template with $\text{Age}/\tau > 4$ and $E(B - V) > 0.25$ were fitted using a dust grid with a maximum value of $E(B - V) = 0.25$. Galaxies morphologically classified as elliptical and S0s required no dust in their SED fits. A complete summary of the parameter space covered by the adopted templates is presented in Table 2. Knowing the spectroscopic redshift of our galaxies, we ran ZEBRA+ in the maximum likelihood mode keeping the redshift fixed to the right values. The best fit templates from ZEBRA+ were also used to compute the *k*-correction for each galaxy.

SFRs were computed as $\text{SFR} = M_{galaxy}/t_A$ for constant SFR models, and $\text{SFR} = \frac{M_{galaxy}}{(1 - e^{-t_A/\tau})} \frac{e^{-t_A/\tau}}{\tau}$ for exponentially declining SFHs (with t_A the age of the best fit model.)

In our ZENS analyses we will use the *integrated* galaxy stellar mass, i.e., the mass obtained from the integration of the star formation histories. We estimate that the “actual” stellar mass, derived from the integrated stellar mass by removing the fraction of mass which is returned to the interstellar-medium by the dying stars, differs, on average, by about -0.2 dex from the total one. An assessment of the uncertainty and reliability of the masses derived with ZEBRA+ is given in Appendix A, where we

Table 2

Template library used to derive stellar masses and (s)SFRs with ZEBRA+.

parameter	range of values
Z	0.004, 0.007, 0.01, 0.02 (Z_{\odot}), 0.03, 0.04
τ (Gyr)	0.05, 0.1, 0.3, 0.6, 1, 1.5, 2, 3, 4, ..., 10, ∞
Age (Gyr)	0.01-12
$E(B-V)$	0-0.5

Note. — The properties of the synthetic spectra used to derive galaxy stellar masses and SFRs through fits to the galaxy SEDs. From top to bottom: metallicity, star-formation history time-scale, stellar age (sampled in 150 logarithmic bins) and dust reddening (sampled in 27 steps spaced by 0.01 mag between $E(B-V) = 0$ and $E(B-V) = 0.1$ and by 0.025 mag at higher reddening). Value of dust extinction greater than $E(B-V) = 0.25$ were allowed only in models with $\text{Age}/\tau < 4$ for galaxies classified as non-quiescent (see Section 5).

compare our results with previously published data and present further considerations on other possible systematics.

3.3. Mass completeness of the ZENS galaxy sample

Given the apparent magnitude selection of the 2dFGRS and the 2PIGG group catalog, the raw ZENS galaxy sample is not a mass-complete sample: the $b_j \lesssim 19.45$ magnitude limit of the survey translates into a minimum observed mass which depends on the intrinsic SED of the galaxies and which is thus different for different galaxy types. Galaxies with the highest mass-to-light ratio (M/L) thus set the mass completeness limit of our survey. We infer this limit empirically from the observed M/L of the ZENS galaxies, following an approach similar to that described in Pozzetti et al. (2010). Specifically, for each galaxy we compute the mass that it would have, given its M/L , once reduced in brightness to the survey limiting magnitude, i.e. $\log(M_{lim}) = \log(M) + 0.4(b_j - b_{j,lim})$. As discussed in Pozzetti et al. (2010), deriving the mass limits using the entire galaxy sample can lead to values which are too conservative and not representative of the masses of the typical galaxies with luminosity close the survey limit. For each morphological or spectral galaxy type we therefore used the 30% faintest galaxies to calculate the completeness mass. This is defined as the mass below which lie 85% of the M_{lim} for the faint galaxies, i.e., the mass above which 85% of these galaxies still fulfill the criterion $b_j < 19.45$. This is illustrated in Figure 1 for the three galaxy *spectral* types in which we have classified our ZENS sample in Section 5.

The resulting completeness limits are, respectively, $\log(M/M_{\odot}) > 9.92$, $\log(M/M_{\odot}) > 9.74$ and $\log(M/M_{\odot}) > 9.21$ for quiescent, moderately star-forming and strongly star-forming galaxies. The mass completeness limits for galaxies of different morphological types are $\log(M/M_{\odot}) > 10.04$ for E/S0 galaxies, $\log(M/M_{\odot}) > 9.82$ for bulge dominated spiral galaxies, $\log(M/M_{\odot}) > 9.78$ for intermediate spirals and $\log(M/M_{\odot}) > 9.48$ for late spirals and irregulars, respectively. In the following we will homogenize these

limits and use $M = 10^{10} M_{\odot}$ as the mass limit for the quiescent and morphological early-type galaxies, and $M = 10^{9.5} M_{\odot}$ for star forming and morphological late-type galaxies.

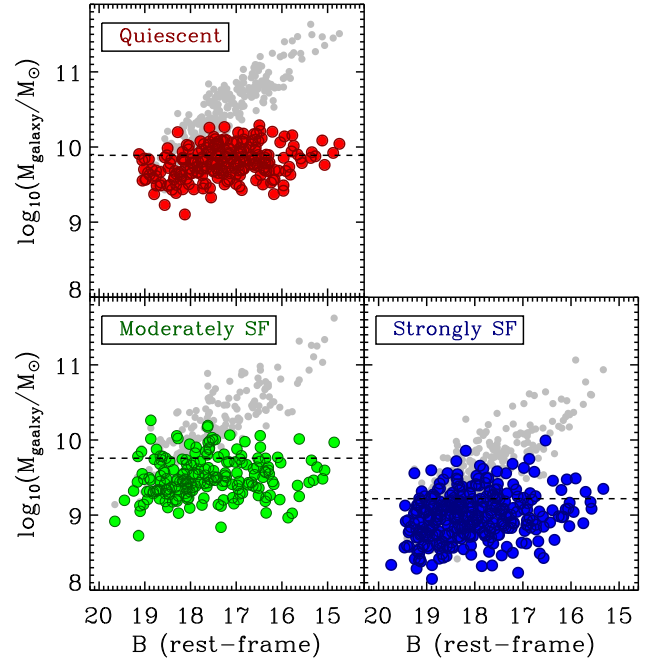


Figure 1. Illustration of the mass completeness derivation for galaxies of the three different spectral types defined in Section 5. The panels show galaxy stellar mass as a function of apparent B -band magnitude, separately for quiescent, moderately star-forming and strongly star-forming galaxies. Small gray dots are galaxy masses inferred from the ZEBRA+ best fits to the photometric data of ZENS galaxies; large colored symbols show the stellar masses obtained by fading galaxies to the 2dFGRS limiting magnitude ($\log(M_{lim}) = \log(M) + 0.4(b_j - b_{j,lim})$; red, green and blue are respectively used for quiescent, moderately star forming and strongly star forming galaxies). The dashed horizontal lines mark the mass completeness limits, defined, separately for each spectral type, as the mass below which lie 85% of the M_{lim} for the 30% faintest galaxies of that given type (see text).

3.4. Variations in median satellite/central galaxy stellar mass across environmental bins

As the main goal of ZENS is to study differential behaviors in similar galaxy populations as a function of several environmental diagnostics, it is essential to keep under control possible variations of galaxy mass distributions in the different environmental bins, as any such variation may induce spurious environmental effects. We thus investigated whether the stellar mass distributions of galaxies of different morphological or spectral types vary with the environmental diagnostics derived for ZENS galaxies in Paper I. Figure 2 plots, from top to bottom, the median galaxy mass of the various morphological and spectral types as a function of group mass M_{GROUP} , distance from the group center (in units of R_{200}) and large scale overdensity δ_{LSS} , considering only galaxies above the completeness limit of each type (i.e., the mass complete samples that will be used in our ZENS analyses). We initially include *all* galaxies of a

given type in this analysis, independent of whether they are central or satellite galaxies. Overplotted in Figure 2, with thick lines in matching colors for the various galaxy samples, are the median galaxy masses of the various morphological and spectral types for the corresponding *satellites only* samples.

The median masses of the different morphological and spectral types for all galaxies are sufficiently constant over the three environments to be confident that our analyses, at a *fixed* galaxy type, will not be biased by strong trends between galaxy stellar mass and any of the ZENS environmental parameters. Small variations of galaxy stellar mass with some of the environments are present for some of the galaxy populations: there is a ~ 0.1 dex increase in the stellar mass of strongly star-forming galaxies with increasing group mass from $\sim 10^{12.5} M_{\odot}$ to $M \gtrsim 10^{14} M_{\odot}$; for this spectral type, a similar mass trends is observed with increasing LSS (over)density, and, for satellite galaxies, when moving closer to the group centers.

For morphologically-split galaxy samples, no trends are observed with group mass. Small trends are in contrast observed for some morphological types with group-centric distance and LSS over-density, i.e., the median mass of E/S0 galaxies is larger by 0.3 dex at small group-centric distances and by 0.15 dex at high LSS densities relative to similar galaxies in the outskirts of groups or at low δ_{LSS} values.

The trends for *satellite* galaxies match quite reasonably those discussed above for *all* galaxies, independent of their satellite/central raking. Specifically, a $\simeq 0.3$ dex increase in galaxy median stellar mass is also observed with decreasing group-centric distance in the intermediate satellite disk galaxy population. If we exclude the central galaxies, overall the mass radial segregation within groups of satellite galaxies is however weak (see also Biviano et al. 2002; Pracy et al. 2005; von der Linden et al. 2010 for a similar result). As pointed out by Peng et al. 2010, the constancy of the characteristic M^* of satellites over a wide range of halo mass, also evidenced in Figure 3, is strong evidence that the mass quenching process for satellites is independent of halo mass, at least above $10^{12} M_{\odot}$. This is because mass-quenching controls the shape of the mass-function of galaxies. Note that, as a consequence of their definition and of our ZENS sample selection, the distributions of galaxy masses for central and satellite galaxies over the common mass range is substantially different, as shown explicitly in Figure 3; furthermore, these two populations overlap basically only at mass scales $\sim 10^{10} - 10^{10.7} M_{\odot}$. We will thus keep this bias into account when comparing the properties of centrals and satellites in our ZENS studies.

4. DERIVATION OF STELLAR MASSES FOR THE BULGES AND DISKS OF TWO-COMPONENTS GALAXIES

In addition to deriving the stellar masses for the entire galaxies as described above, we also estimated stellar masses separately for the bulge and disk components of disk galaxies with bulge/disk decompositions available from Paper II from GIM2D decompositions. To this purpose, we converted the $(B - I)$ colors of bulges and disks into an I -band mass-to-light ratio (M/L) by using a set of stellar population models from the Bruzual & Charlot (2003) library, constructed with a Chabrier ini-

tial mass function. We adopted as our fiducial M/L for the galaxy components the median M/L obtained from fitting all the synthetic spectra.

We employed simple stellar population models (SSP) as well as exponentially decreasing star-formation histories, with characteristic time scales of $\tau = 1, 3, 6$ Gyr. For each star-formation history we used the range of metallicities $Z=0.004, 0.005, 0.008, 0.01, 0.02, 0.03, 0.05$, in units such that 0.02 is the Solar metallicity (Z_{\odot}). Another set of models, based on the same grid of parameters, was reddened with a Calzetti dust law and $E(B - V)=0.05, 0.1, 0.15, 0.2$. Dust-reddened models were used only for galaxies that were classified as star forming systems (see Section 5).

A k -correction is needed to convert the bulge and disk apparent magnitudes into rest-frame luminosities. Whereas for the entire galaxies we can calculate these corrections from the UV to near-infrared (NIR) SED fits of ZEBRA+, such information is not available for the bulges and disks for which we have only the B - and I -band photometry. For this reason, we performed a linear fit to the relation between the apparent $(B - I)$ color and the ZEBRA+ k -corrections as obtained for the entire galaxies, and we used this average relation to infer the k -corrections for the galaxy components. Consistently with the definition adopted for the galaxies, we consider in the following total stellar masses for bulges and disks, which include also the fraction of baryons which is returned as gas to the ISM as stars evolve.

To assess the reliability of the derived masses of bulges and disks, in Figure 4 we compare the total galaxy stellar masses derived in Section 3 with the sum of the stellar masses of their bulge and disk components. We highlight with red and blue symbols respectively elliptical galaxies and pure disk galaxies, i.e., galaxies for which a two-component GIM2D fit returns as the best fit a model with $B/T = 0$. The Figure shows a very good agreement with a scatter of ~ 0.18 dex, comparable with the average error on the total galaxy mass estimate (see Appendix A).

5. DEFINITION OF GALAXY SPECTRAL TYPES: QUIESCENT, MODERATELY STAR-FORMING AND STRONGLY STAR-FORMING GALAXIES

The split between quiescent and star-forming galaxies is a rather arbitrary one, for many reasons. First, it is plausible to expect that, in nature, star formation activity is a continuum property of galaxies, and the distinction between the two populations is not a dichotomy. Second, observational biases such as a threshold of detectability of star formation rates in any given survey can affect the classification. In ZENS we try to clean, as much as possible, our quiescent/star-forming classification of galaxies in the sample, by adopting an approach that combines three different probes of star formation activity, namely (i) the original 2dF spectra, (ii) FUV-NUV-optical colors, and (iii) the SFR estimates from the SED fits to the galaxy photometry described above. The main philosophy that we adopt is to automatically classify a galaxy as star-forming or quiescent when all the three diagnostics agree on the classification, and to explore all diagnostics to understand what causes discrepancies when these arises. We end up with a three-bin classification in quiescent, moderately star forming

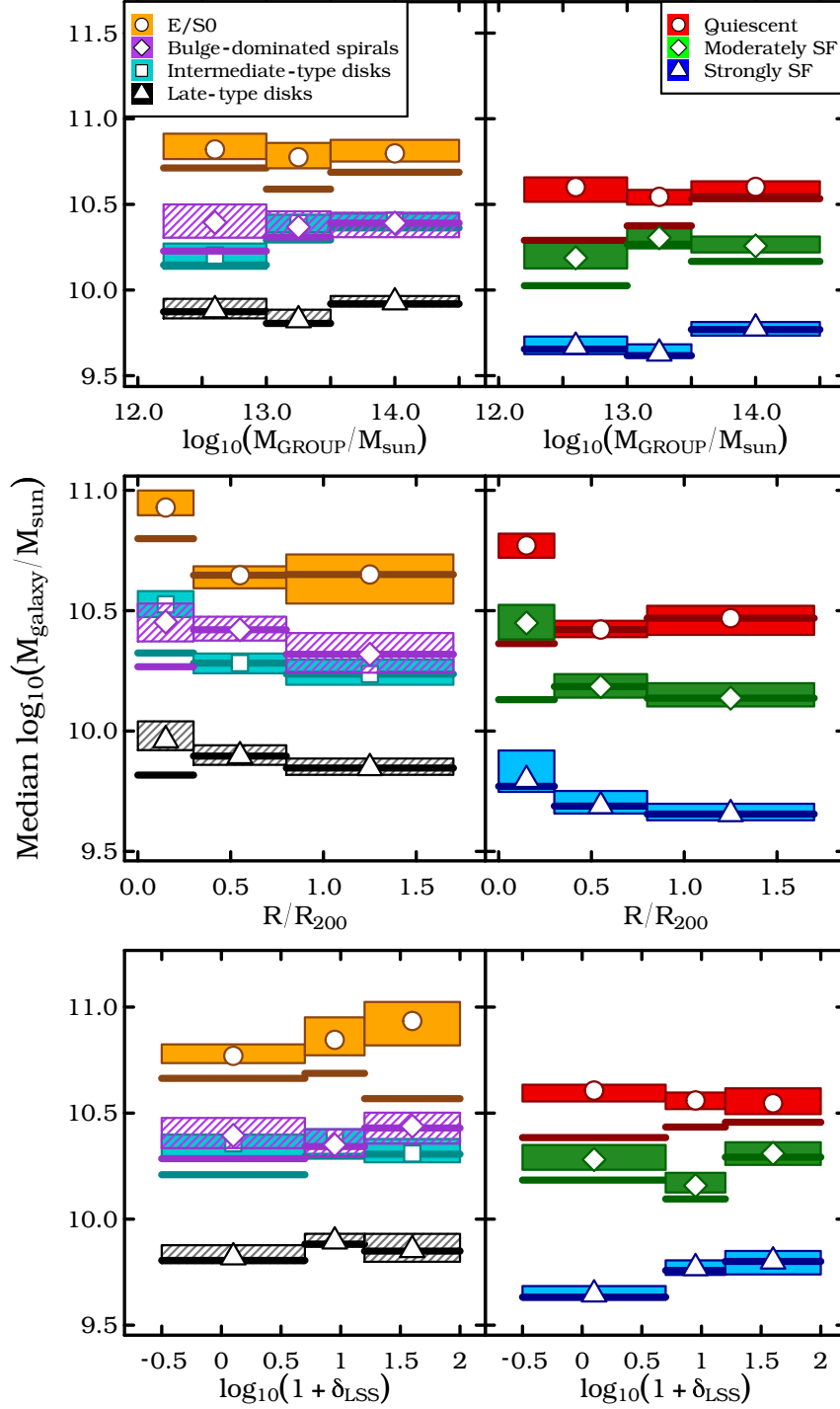


Figure 2. Median galaxy stellar mass as a function of environment for galaxies of different morphological (left) and spectral types (right; see legends for details). From top to bottom the considered environments are group halo mass, distance from the group center and large scale density. Median values are calculated above the mass completeness of each spectral/morphological type. Error bars represent the standard deviation of the median masses computed from the 16th and 84th percentiles. Colored boxes with white open symbols indicate samples including *all* galaxies, independent of their rank as centrals or satellites. The thick solid lines in matching colors are the results for *satellites only* samples.

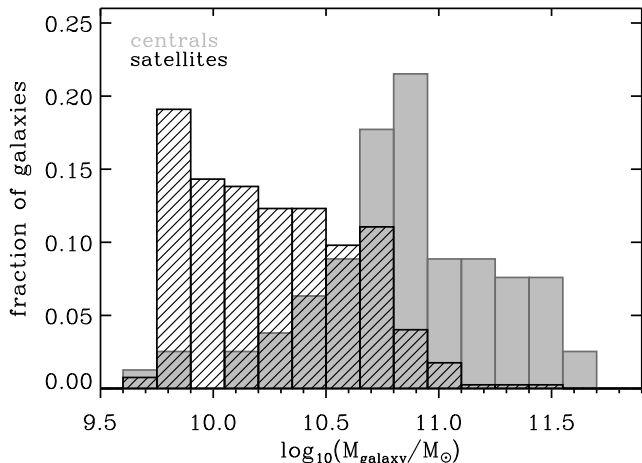


Figure 3. Distributions of galaxy stellar masses for central (filled, grey histogram) and satellite galaxies (black, hatched histogram), over the mass range spanned by the central population. Each histogram is normalized to its sum.

and strongly star forming galaxies, the last two classes being broadly diversified by the level of the specific star formation rate measured by the SED fits. We detail our classification procedure below.

5.1. First constraint to the spectral classification: Line features in the 2dFGRS spectra

The 2dFGRS team provides for each galaxy the spectral indicator η (Madgwick et al. 2002) which characterizes the activity of the galaxy. The parameter η correlates by definition with the intensity of the emission lines (most strongly with the equivalent width of $H\alpha$); however, it does not contain detailed information on which species are in emission nor their relative strength, aspects which are important to identify mixed types or galaxies in which the emission is powered by an AGN rather than by star formation. Furthermore, we worried that the fibers of the 2dFGRS spectrograph, having a fixed diameter of $2'' - 2.16''$, probe a different fraction of the galaxy light depending on the galaxy’s apparent radius. Whereas for a good fraction of the ZENS galaxies the $2''$ aperture is large enough to cover a significant part of the galaxy, for others the spectrum is only probing the inner most region, leaving scope for misclassifications. We thus individually inspected ourselves the 2dFGRS spectra of the ZENS galaxies to study the emission and absorption line features in the galaxy spectra.

A relative flux calibration for the spectra was obtained by using the average response function and telluric corrections available on the 2dFGRS web-site¹⁰. A boxcar-averaged continuum (over 250 pixels) was subtracted from the spectra before performing the visual inspection. The wide wavelength coverage of the 2dFGRS spectra and the low redshifts of our galaxies allow us to look for a number of star-formation tracers, i.e., hydrogen $H\beta$ and $H\alpha$ Balmer lines, and forbidden transitions of [OII] $\lambda 3727$, [OIII] $\lambda 5007$, and [NII] $\lambda 6584$.

¹⁰ These are the *eff-pop-syn-mid.dat* and *eff-telluric.dat* files, respectively. We did not attempt an absolute flux calibration of the spectra, which is beyond our purposes.

Based on the spectral information, we classified a galaxy as *quiescent* if its spectrum satisfies one of the following conditions: a) none of the aforementioned lines is observed in emission, or b) some [OII] / [NII] emission is present but no $H\beta$ or $H\alpha$ is detected. It is not unusual to observe [OII] or [NII] emission in ellipticals or in galaxies on the red sequence (e.g. Caldwell 1984; Phillips et al. 1986; Macchetto et al. 1996), but the presence of this ionized gas is often a consequence of AGN or LINER nuclear activity rather than as a signature of star-formation spread across the entire galaxy (Yan et al. 2006; Annibali et al. 2010; Lemaux et al. 2010).

Galaxies were classified as star-forming if they showed strong emission in all four of the above species. Emission-line spectra can have large contributions from active galactic nuclei (AGNs) (Heckman 1980; Baldwin et al. 1981; Veron et al. 1997; Kauffmann et al. 2003). A widely used method to identify AGNs, first proposed by Baldwin et al. (1981) and revised in several later works (e.g. Veilleux & Osterbrock 1987; Tresse et al. 1996), relies on the relative strength of the [NII]/ $H\alpha$ and [OIII]/ $H\beta$ line ratios. We used this diagnostic to identify AGN candidates in our sample and flag them in the ZENS catalog.

In the next Section we describe how we further split star forming galaxies into two classes of, respectively, *strongly star forming* and *moderately star forming* systems. The latter identify a transition galaxy type with modest star formation activity in between that of strongly star-forming and quiescent galaxies. This transition class is defined on the basis of an NUV-optical color cut; an a posteriori check of the 2dF spectra of these galaxies shows indeed that they have typically intermediate spectra between those of strongly star-forming and quiescent galaxies.

The stacked spectra of the three spectral types are shown in Figure 5. Clearly visible is the transition from a spectrum dominated by stellar absorption for the quiescent galaxies, to a spectrum dominated by nebular lines for the strongly star-forming galaxies. The moderately star-forming galaxies present weaker emission lines than those observed in the strongly star-forming galaxies; as also highlighted below, they also have a redder continuum in comparison to this latter class. In Figure 5 we also indicate the median value of the 2dFGRS spectral parameter η for the three classes: in about 90% of the galaxies we find a good agreement between our classification and the one provided by the 2dFGRS team, with the remaining discrepancies due to spectral misidentifications, as discussed above.

5.2. Second constraint to the spectral classification: FUV-NUV-optical broad-band colors

The combination of FUV/NUV and optical/NIR colors has been shown to be a powerful tool to disentangle dust-reddened star-forming galaxies from red-and-dead quiescent galaxies (Gil de Paz et al. 2007; Haines et al. 2008; Williams et al. 2009; Bundy et al. 2010). As an independent validation of the spectral classification of the ZENS galaxies presented above, we analyzed the two color-color diagrams illustrated in Figure 6, i.e., the $(NUV - I)$ - $(B - I)$ and the $(FUV - NUV)$ - $(NUV - B)$ diagrams. To this purpose we used the aperture photometry described in section 3.1; rest-frame magnitudes were obtained using the k -corrections derived from the ZEBRA+ best-fit

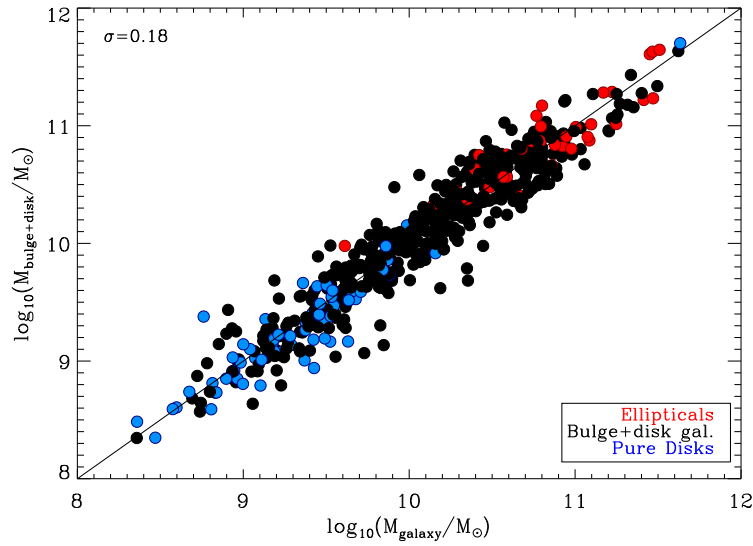


Figure 4. Comparison between galaxy stellar masses derived from the SED fits to the galaxies photometric data, and galaxy stellar masses obtained by summing up the separate contributions of their bulges and disks. Bulge and disk stellar masses are inferred from the GIM2D bulge+disk decompositions of Paper II, using the $(B - I)$ colors of these components as proxies for their M/L values. Elliptical galaxies are shown in red, and single-exponential (i.e., “pure”) disk galaxies in blue; galaxies with both a bulge and a disk component are shown in black. The two mass estimates show a very good agreement within a scatter of $\sigma = 0.18$ dex.

SEDs.

We used Bruzual & Charlot (2003) (BC03) models to determine suitable color cuts in these diagrams for a three-bin spectral classification as above. Specifically, the condition for galaxies to be classified as quiescent was set to: $NUV - I > 4.8$, $NUV - B > 3.5$ and $B - I > 1.2$; these color cuts identify >5 Gyr passively evolving SSP models (grey lines in the figure). Strongly star-forming galaxies were defined to have $NUV - I < 3.2$, $NUV - B < 2.3$ and $B - I < 1.0$, i.e., cuts which are consistent with the colors of 1-5 Gyr-old stellar populations with a $\tau = 1$ Gyr exponentially declining star-formation history (black lines). Moderately star-forming galaxies are shown with green points in Figure 6 and were selected to have NUV-optical colors that fall between the two bracketing classes above.

The reddening arrow in the $(NUV - I)$ - $(B - I)$ diagram moves galaxies parallel to the sequence defined in this diagram by the star-forming galaxies, but away from the region occupied by the quiescent galaxies. In contrast with the degeneracy observed for optical colors, the NUV-optical color-color diagram is thus particularly effective in discriminating dusty star-forming galaxies from passively evolving galaxies. Note that we do not use the FUV passband as a classification criterion, but its availability enables us to define a FUV-NUV color in the vertical axis of the right panel of Figure 6, which gives a further handle to verify the robustness of the different spectral types.

The filled red and blue symbol in Figure 6 show galaxies that satisfy both the spectral *and* color conditions that are required for qualifying quiescent and strongly star forming galaxies, respectively. Empty symbols indicate galaxies which do not satisfy simultaneously both classification criteria, but are assigned to one of the two classes following a visual inspection of the spectra and

images. There are two categories of such objects: galaxies with a quiescent spectrum but “blue” colors relative to normal quiescent galaxies, and galaxies with a strongly star-forming spectrum but with redder colors than normal star forming galaxies. Note that “red” galaxies with a star-forming spectrum are nevertheless generally bluer than the red-and-dead quiescent population. Most of the red star-forming galaxies are disks with a relatively high inclination, i.e. ellipticity $\epsilon > 0.4$ (see Figure 7). The red colors of these object are a consequence of dust obscuration. A possibility for the bluer-than-normal colors in some of the quiescent galaxies is that the fiber-spectra catch only the light of a quiescent bulge, and leave star formation in an outer disk undetected. The analysis the WFI B and I images shows that this is the case for four galaxies in the first-epoch ZENS data. In the remaining cases, quiescent “blue” galaxies may possibly have had a minor episode of star-formation which is causing the integrated color to become slightly bluer, or may have passively evolving populations that are on average younger than those of their redder counterpart. We flag these galaxies as potential “post starburst” in the ZENS catalog.

Combining the spectroscopic analysis discussed in the previous Section with the (FUV and) NUV-optical photometric diagnostics leads to a robust spectral classification for the ZENS galaxies in the three classes of quiescent, moderately star forming and strongly star forming galaxies. This classification however does not provide a quantitative estimate for the SFRs of the galaxies, for which we do rely on the ZEBRA+ SED fits. We therefore assessed, as described below, whether such SFR estimates are consistent with the spectral classification of the ZENS galaxy sample.

5.3. Quantitative SFRs from ZEBRA+ SED fits

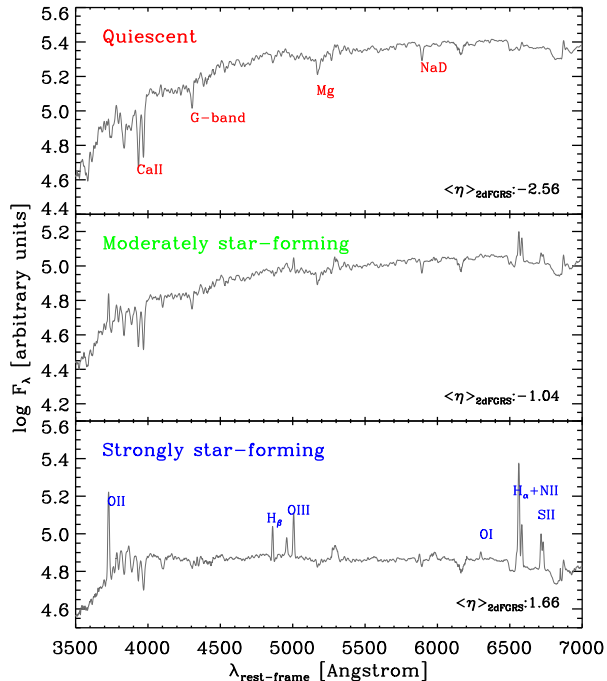


Figure 5. Stacked spectra of the ZENS galaxies classified as quiescent, moderately star-forming and strongly star-forming. The main emission/absorption features are indicated on top of the upper and lower panels. Quiescent galaxies are characterized by strong stellar absorption lines and an underlying red continuum; star-forming galaxies have a blue continuum and intense nebular emission. The moderately star-forming type have properties which are intermediate between these previous two classes. Each composite spectra is obtained from $\gtrsim 200$ individual spectra. The flux is given in logarithm of raw counts, hence the absolute normalization is arbitrary. The median value of the spectral parameter η provided with the 2dFGRS database for the three spectral types is indicated on the bottom right of the panels. Note that in the original 2dFGRS classification scheme, quiescent galaxies have $\eta < -1.4$, star-forming galaxies $\eta > -1.4$ and star-bursts $\eta > 3.5$.

The top panel of Figure 8 shows the relation between specific star formation rate (i.e., SFR/M_{galaxy} ; hereafter sSFR) and galaxy stellar mass M_{galaxy} , with highlighted in red, green and blue the three spectral classes discussed above (color coding as in Figure 6). Not surprisingly and reassuringly, there is a very good agreement between the quantitative SED-based SFR estimates and the assigned spectral types. Galaxies classified as quiescent based on their absorption spectral features and/or red NUV-optical colors have generally $\log(\text{sSFR}/\text{yr}) \lesssim -11$, i.e., at their current star-formation rates, it would take more than 10 times the present age of the Universe (t_U) to double their mass. Strongly star-forming galaxies have $\log(\text{sSFR}/\text{yr}) \gtrsim -10$, i.e., mass-doubling times much shorter than t_U ; moderately star-forming galaxies fall in between the two bracketing classes. It should be noted that the sample in 8 includes quiescent galaxies, and is not complete in stellar mass at the low end, and so the steep slope of the sSFR-mass relation indicated in the Figure should not be taken to indicate a highly negative

value of β in the relation $\text{sSFR} \propto M^\beta$ (c.f. Peng et al. 2010).

We highlight that in the first-epoch ZENS sample, there are 21 galaxies that are classified as moderately or strongly star-forming systems based on their spectral features and/or colors, but whose initial, unconstrained ZEBRA+ best fits resulted in incorrectly low (specific) star-formation rates ($\log(\text{sSFR}) < -11.8$). We explored the origin of this inconsistency. For 11 of these “problematic” galaxies no GALEX photometry is available, and thus for them a reduced number of passbands was used to perform the SED fits, which are unconstrained at UV wavelengths. The remaining 10 galaxies were found to have high inclinations thus the too low sSFR are likely the result of an underestimation of the amount of dust reddening in such galaxies (the typical reddening is $E(B - V) = 0.08$ in the unconstrained fits). For all these galaxies, we thus re-run our ZEBRA+ fits constraining the latter to a star-forming SED model, specifically by only using constantly star-forming templates (csf) or templates with an exponentially decreasing star-formation history with $\tau = 2, 4, 6, 8$ Gyr and ages between 0.4 and 4 Gyr. The same metallicity and reddening as in Table 2 were used for these ‘constrained’ ZEBRA+ runs. This led to revised SFR, stellar mass and sSFR estimates (magenta symbols in Figure 8) for these 21 galaxies¹¹, which are flagged in the ZENS catalog that we have published in Paper I. As expected, the revised stellar masses are slightly larger (on average by 0.15 dex) than the mass estimates providing the clearly incorrect (i.e., too low) sSFRs. The column in the ZENS catalog that is used as a flag to identify these galaxies lists the “incorrect” galaxy stellar mass values for these 21 galaxies (and a dummy entrance for the remaining ones); the column listing SFRs and sSFRs incorporate the “correct” values, obtained with the star-forming SED templates of the constrained ZEBRA+ fits. When appropriate, we will test our analysis excluding these galaxies from our sample.

We then used the morphological classes established in Paper II to examine the morphological mix within each of the spectral type; these morphological mixes are listed in Table 3 and shown in the middle panel of Figure 8, which again plots the sSFR-mass relation as before, with highlighted in different symbols galaxies of the various morphological classes (with colors still representing the spectral type as before). As expected, there is a broad correlation between morphological and spectral types, i.e., E/S0 galaxies are largely quiescent, and morphologically-classified late-type disks are mostly strongly star-forming galaxies. Intermediate-type disks distribute themselves almost equally in the three spectral classes, and a third of the bulge-dominated spiral galaxies shows some star-formation activity. We discuss in more detail in Paper IV (Lu et al. 2012) the morphological properties of quiescent and star forming galaxies and the dependence of

¹¹ These galaxies are 2PIGG_s1282_4, 2PIGG_s1349_5, 2PIGG_s1418_2, 2PIGG_s1677_6, 2PIGG_n1365_3, 2PIGG_n1394_1, 2PIGG_n1398_2, 2PIGG_n1440_16, 2PIGG_n1441_13, 2PIGG_n1467_5, 2PIGG_n1476_1, 2PIGG_n1588_20, 2PIGG_n1588_26, 2PIGG_n1588_37, 2PIGG_n1588_46, 2PIGG_n1588_53, 2PIGG_n1588_71, 2PIGG_n1593_8, 2PIGG_n1648_2, 2PIGG_n1702_8, 2PIGG_n1829_61.

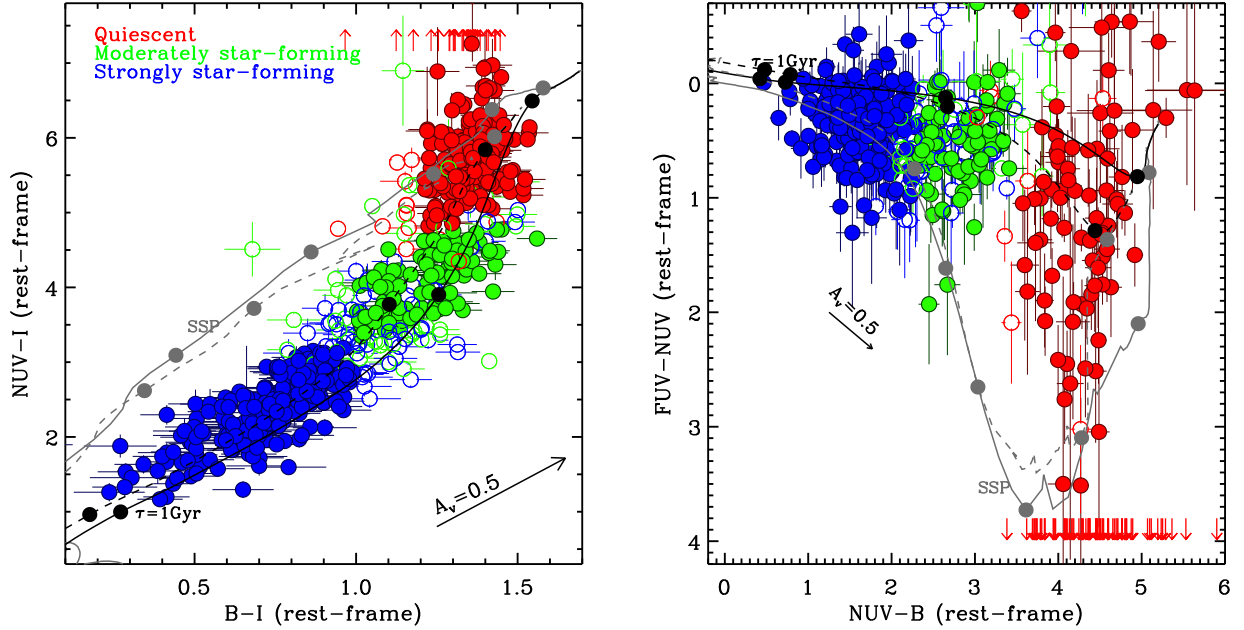


Figure 6. Color-color diagrams used, together with the original 2dF spectra, to classify ZENS galaxies in the three spectral types of strongly star-forming, moderately star-forming and quiescent galaxies. *Left panel:* Rest-frame $(NUV - I)$ - $(B - I)$ color-color diagram. Quiescent galaxies are shown in red circles, moderately star-forming galaxies in green and strongly star-forming galaxies in blue. Filled points show galaxies which satisfy all color and spectral criteria used to define these classes; empty symbols are galaxies which do not meet some of the constraints but are assigned a given class after visual inspection of the spectral and imaging data. Red arrows show quiescent galaxies which are undetected in the NUV ; these are positioned at an arbitrary value along the vertical axis for visualization purposes. The lines are predictions for the color evolution of two synthetic models from the Bruzual & Charlot (2003) library, i.e., an SSP (grey) and an exponentially declining star-formation history with an e-folding time of 1Gyr (black lines) with a metallicity of $Z = Z_{\odot}$ (solid lines) and $Z = 0.4Z_{\odot}$ (dashed lines). From left to right, the large black circles indicate the colors of these stellar populations at the ages of 0.5, 1, 5 and 10 Gyr. The effect of a $A_V = 0.5$ dust reddening vector is shown with an arrow. Conversion to rest-frame colors is obtained using the k -correction values given by the ZEBRA+ best-fit templates. *Right panel:* $(FUV - NUV)$ - $(NUV - B)$ color-color diagram. Symbols and lines are as in the left panel.

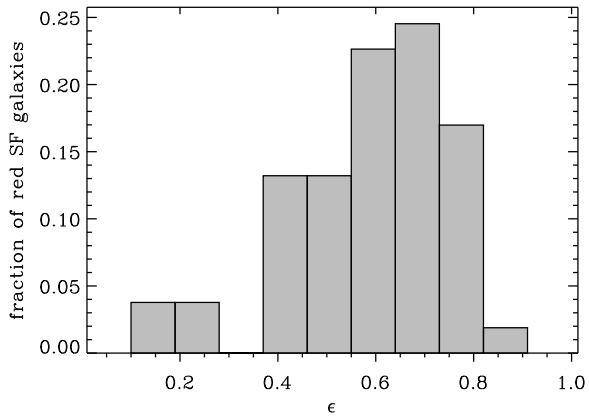


Figure 7. Distribution of ellipticities for galaxies which are classified as strongly star-forming based on the 2dF spectra, but which have red optical or NUV-optical colors. The majority of these galaxies have large ellipticities; also at a visual inspection, they are disk galaxies with large inclination angles. Thus we attribute the reddening of their colors to dust obscuration.

the passive fraction on the different environments that we study in ZENS.

Finally, the bottom panel of Figure 8 explicitly shows that, although quiescent galaxies segregate into a tight red sequence, defined by our color cut $(B - I) > 1.2$,

and moderately- and strongly star-forming galaxies are respectively mostly located in “green-valley” and “blue-cloud” regions, both star-forming classes have $(B - I)$ colors that overlap with the red sequence of quiescent galaxies. This is further illustrated in the left panel of Figure 9, showing the sSFR vs. integrated $(B - I)$ color, and, explicitly, in the right panel of the same figure, which quantifies the contamination of star-forming galaxies to the red sequence, as defined though the $(B - I)$ color. Specifically, the right panel of Figure 9 shows, as a function of stellar mass, the fraction of galaxies which are classified as either strongly star-forming or moderately star-forming and have colors $(B - I) > 1.2$ (normalized to the total number of galaxies with such $(B - I)$ colors). We note that the relative importance of dust-reddened galaxies increases with decreasing stellar mass; dust-reddened strongly and moderately star forming galaxies together are $\sim 50\%$ of the nominal red sequence at our completeness mass limit for quiescent galaxies of $10^{10}M_{\odot}$. This result is supported by independent analyses at similar mass scales (e.g. Bell et al. 2004; Davoodi et al. 2006; Haines et al. 2008; Maller et al. 2009).

6. $(B - I)$ TWO-DIMENSIONAL COLOR MAPS AND RADIAL COLOR GRADIENTS

To study the variation of stellar populations and distribution of star-forming regions within galaxies, we used the WFI B and I images to construct a two-dimensional

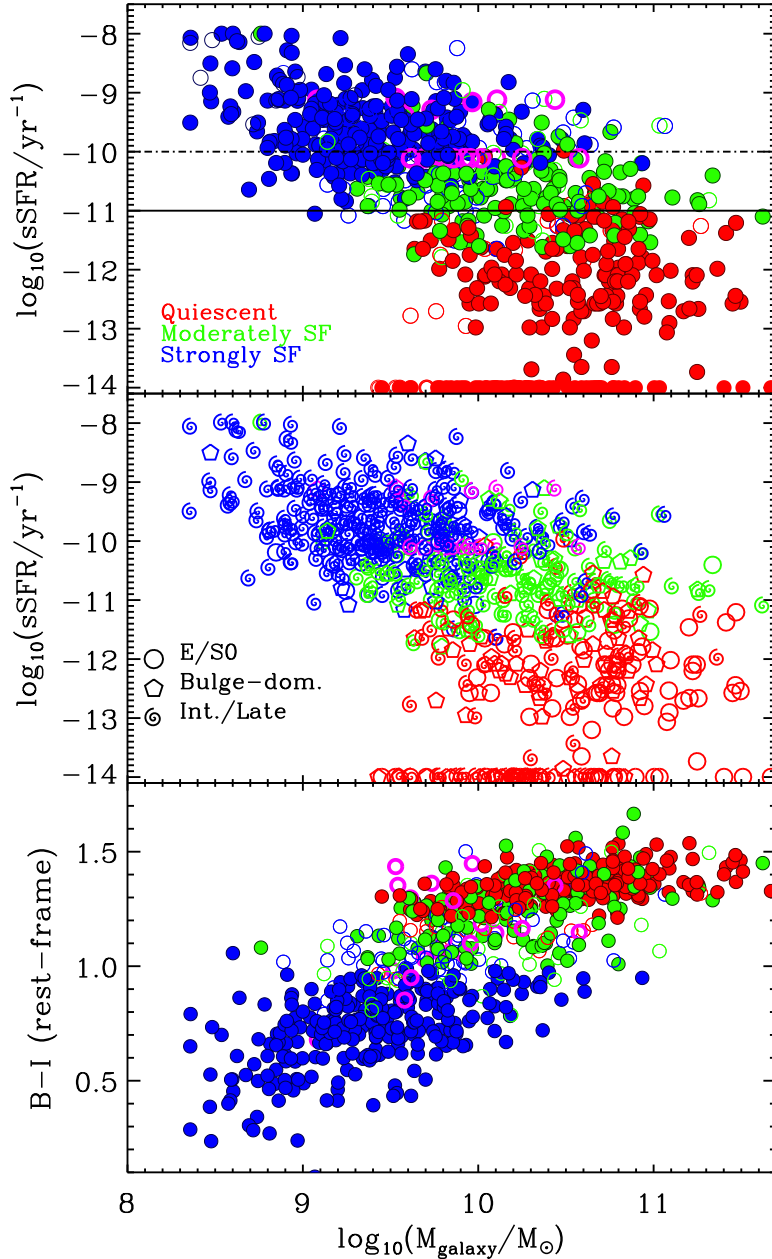


Figure 8. *Top:* Location of the three spectral types on the sSFR vs. galaxy stellar mass relation. Symbols and colors are as in Figure 6. The horizontal dashed and solid lines mark the inverse of the current age of the Universe and ten times the current age of the Universe, respectively. The 21 galaxies with “enforced” star-forming SED templates discussed in the text are identified with magenta (empty) symbols. Galaxies plotted at a constant $\log_{10}(\text{sSFR}/\text{yr}) = -14$ are quiescent systems for which the best fit SED model resulted in very low star-formation rates ($\text{SFR} < 10^{-4} M_{\odot} \text{yr}^{-1}$). *Middle:* Symbols in this panel correspond to different morphological types: ellipticals and S0s are shown with circles, pentagons are for bulge-dominated spiral galaxies and intermediate-/late-type disks are shown with spiral symbols; color are as before. *Bottom:* $(B - I)$ color vs. galaxy stellar mass. Symbols and colors are as in the top panel of the figure.

$(B - I)$ color map for each galaxy. Since the B and I filter observations have different point spread functions, we cross-convolved each passband with the PSF of the other passband. To prevent spurious color gradients arising from errors on the registration of the two images, we rebinned the original pixels in 7×7 sub-pixels before performing the registration of the B - and I -images using the IRAF task `imalign`. A correction for Galactic dust extinction was applied to the color maps.

6.1. Voronoi tessellation

To increase the S/N of the color maps in the outer regions of a galaxy, where the flux from the sky background is dominant, we performed an adaptive local binning of pixels using a *Voronoi tessellation* (VT) approach.

The idea behind the method is to group adjacent pixels into bigger units that have a minimum scatter around a desired signal-to-noise ratio (*uniformity requirement*).

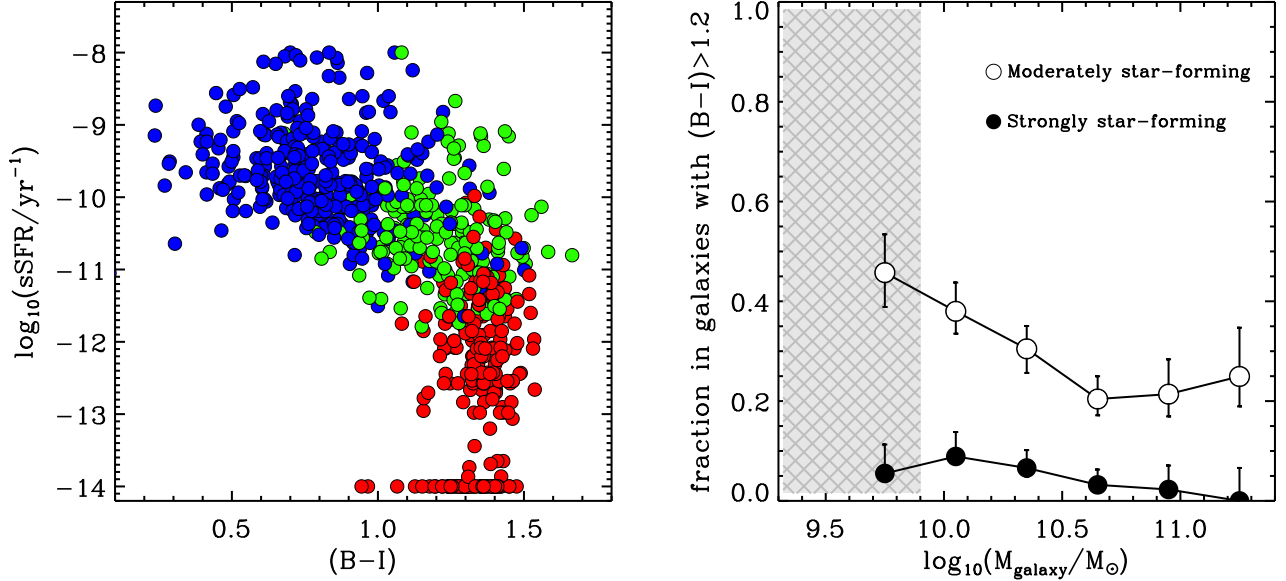


Figure 9. *Left:* sSFR as a function of galaxy integrated $(B - I)$ color. Symbols are color coded according to the spectral type as in Figure 8 (galaxies plotted at a constant $\log_{10}(\text{sSFR}/\text{yr}) = -14$ are systems for which the best fit SED model resulted in very low star-formation rates, $\text{SFR} < 10^{-4} M_{\odot} \text{yr}^{-1}$). *Right:* Fraction of galaxies with $(B - I) > 1.2$ (i.e., contaminants to the “optical red-sequence” of passively evolving galaxies) which are classified as strongly star-forming (filled symbols) or moderately star-forming (empty symbols). The grey shaded area show the region of mass incompleteness for quiescent galaxies in the ZENS sample.

Table 3
Morphological mix for the three spectral classes in the ZENS sample

Morphological Type	% Quiescent	% Moderately-SF	% Strongly-SF
Es	100%	-	-
S0s	93%	7%	-
Bulge-dominated spirals	64%	21%	15%
Intermediate-type disks	39%	34%	27%
Late-type disks	3%	25%	72%
Irregulars	-	-	100%

Note. — For each of the morphological types of Paper II, the table lists the corresponding fractions for the different spectral types discussed in Section 5.

The tessellation should further satisfy a *topological* and *morphological* requirement, i.e., create a partition without gaps or overlapping regions and a maximum roundness of the bins should also be attained. In the VT technique a density distribution of the signal-to-noise ratio over the area of the galaxy is defined, $\rho(r) = (S/N)^2(r)$, and binning to a constant S/N is then ensured by determining regions of equal mass according to ρ . The VT method is often used to maximize the reliability of astrophysical information from noisy data (albeit at the expense of angular resolution; see e.g. Ferreras et al. (2005); Daigle et al. (2006)).

To perform the VT on the $(B - I)$ color maps of the ZENS galaxies we used the publicly available IDL codes of Cappellari & Copin (2003)¹² and in particular we adopted the generalization (*weighted voronoi tessellation (WVT)*) proposed by Diehl & Statler (2006). For the code to work, along with the color map it is necessary to

provide an estimate of the signal-to-noise of each pixel. We computed the error on each pixels using the cross-convolved images as $\sigma = 1.0857 \frac{\sigma_{flux}}{\langle I \rangle}$. Here $\langle I \rangle$ is the intensity in counts measured from the source. The flux error is the sum of poisson fluctuations in the number of photons from the source plus random noise from the sky, i.e., $\sigma_{flux} = \sqrt{\langle I \rangle / g_{eff} + \sigma_{sky}^2}$ where g_{eff} is the effective gain of the image and σ_{sky} the standard deviation of the background; the use of the effective gain takes into account that poisson statistics applies to the total number of electrons coming from the sources. Error on the pixels of color maps were then obtained by adding in quadrature the errors in the two filters.

Pixels with very low S/N ratios, which would affect the robustness of the algorithm, were excluded from the binning by imposing a minimum threshold of $S/N^2 = 0.05$, found to optimize the results. Pixels belonging to the background, defined as pixels at a distance > 1.5 Petrosian radii from the center of the galaxy, were also re-

¹² <http://www-astro.physics.ox.ac.uk/~mxc/idl/>

jected by using a mask image. A target S/N ratio of 10 was chosen to construct the binned color maps.

Figure 10 shows the comparison between the original, un-tessellated color maps and the VT maps, together with the azimuthally-averaged signal-to-noise and color radial profiles derived from the original and tessellated images. The three galaxies in the figure are representative of the variety of observed color profiles: a galaxy with a negative color gradient (redder center, bluer outskirts), a galaxy with a flat color profile and a galaxy with a positive color gradient (blue center, redder outskirts). The VT clearly enables a more robust measurement of the color distribution of galaxies at large radii, and removes the high frequency fluctuations associated with the noise in the original color maps, while retaining substantial information on lower frequency, physical color variations within galaxies.

6.2. Azimuthally-averaged radial $(B - I)$ color profiles

Azimuthally-averaged $(B - I)$ color profiles for the ZENS galaxies were obtained both from the tessellated color maps and from the GIM2D B and I -band single-component Sérsic fit parameters derived and calibrated in Paper II (to which we refer for details of the fits and their calibration against residual PSF, ellipticity and concentration biases). The advantage of the former approach is that color profiles from the color maps are a straight measurement from the data and are thus not affected by data-model mismatches; the advantage the latter approach is the substantial removal of observational biases, including PSF smearing, which enables in principle to study color profiles also within the PSF radius.

Logarithmic color gradients were in both cases calculated by fitting the linear relation $(B - I) = (B - I)_{r_{1/2}} + \alpha \log(r/r_{1/2})$ to the color radial profiles. The slope $\alpha = \Delta(B - I)/\Delta(\log r) \equiv \nabla(B - I)$ defines what we will refer to as the “radial color gradient”; $(B - I)_{r_{1/2}}$ defines the color at the galaxy half-light semi-major axis ($r_{1/2}$). These $(B - I)_{r_{1/2}}$ colors were converted from observed to rest-frame using the k -correction derived from the ZEBRA+ fits.

Unless obvious, we will distinguish in the following and future papers between gradient parameters derived from the GIM2D analytic fits and those obtained from the VT color maps by adding the subscripts “GIM2D” and “Voronoi” to the symbols $\nabla(B - I)$ and $(B - I)_{r_{1/2}}$. Note that the agreement between the parameters of the color profiles obtained with the two approaches was found to be generally good; where systematic differences were identified, we studied the origin of such discrepancies and derived recipes to tie the two measurements to a common scale, as described in Section 6.2.1. We adopt as our fiducial measurements in our future ZENS analyses the radial color profiles $\nabla(B - I)_{GIM2D}$ based on the analytical Sérsic fits; these fits were performed within the radial range $0.1r_{1/2} - 2.5r_{1/2}$. We will use however the parameters $\nabla(B - I)_{Voronoi}$ and $(B - I)_{r_{1/2},Voronoi}$ derived from the VT color maps for the 5% of ZENS galaxies for which no analytical fit could be derived, and also as a check of the analytical color profiles at relatively large radii ($> FWHM_{PSF}$).

The empirical “Voronoi” radial color profiles are affected by observational biases, and require therefore some

corrections. We detail below the main issues involving these estimates for the radial color profiles, and the approaches that we have taken to minimize spurious observational effects in their estimates.

Finally, we note that the VT color maps contain more information than one-dimensional gradients; in particular, they enable us to study also the color r.m.s. dispersion (scatter) around the smooth average color profiles within galaxies. This was defined and computed as $\sigma(B - I) = \sqrt{\sum_i \xi_i^2 / N}$, with ξ residuals with respect to the azimuthally-smoothed radial color profile.

6.2.1. Color profiles and color scatter from the VT color maps: Corrections for systematic effects

Fits to the color profiles based on the VT color maps were limited between $r_{PSF} < r < r_{MAX}$, with r_{MAX} either $2.5 \times r_{1/2}$ for sufficiently high S/N maps, or the maximum radius over which the tessellation could be performed. The inner profile within the radius r_{PSF} , equal to the largest between the B and I seeing FWHM, was masked out to minimize the effects of PSF-blurring. We assumed that, on large scales, the radial distribution of color in the galaxies is axisymmetric and joined together all the Voronoi bins which are crossed by the same ellipse of given semi-major axis when deriving the color profiles. Strong outlying Voronoi cells (produced by, e.g., bright star-forming regions) were masked out from the fits. These outlier cells were defined as those with colors > 5 -sigma away from a biweighted mean of the colors of all Voronoi cells, or > 3.5 -sigma away from the best-fit linear regression to all cell colors as a function of radius. Radial color gradients $\nabla(B - I)_{Voronoi}$ and $(B - I)_{r_{1/2},Voronoi}$ colors were then calculated with a Levenberg-Marquardt least-squares fit to the remaining Voronoi cells data.

As anticipated, the VT-based radial color gradients require some corrections. Not least, galaxy to galaxy variations prevent an homogeneous radial sampling of the color gradients amongst the entire sample: the minimum radius which is probed depends on the seeing under which a given galaxy was observed, and the maximum radius is often set by the noise of the image and the galaxy brightness and intrinsic size. Figure 11 shows the distribution of these minimum and maximum radii employed in the calculation of the color gradients from the Voronoi maps, in units of the galaxies half-light radii. Rather comforting is that, for most of the sample, the fitted region spans a range of radii from well below $r_{1/2}$ up to $\sim 2.5 \times r_{1/2}$; in only 8% and 3% of the galaxies the minimum radius is larger than $0.7r_{1/2}$ and the maximum radius is smaller than $1.3r_{1/2}$, respectively. Note that as shown on the inset in Figure 11 these two troublesome situations, however, never occur at the same time.

Also, PSF blurring and consequent masking of the central galactic regions (by one PSF’s FWHM) remain a source of concern for the reliability and stability of the derived $\nabla(B - I)_{Voronoi}$ values. In Figure 12 we plot the gradients $\nabla(B - I)_{Voronoi}$ as a function of r_{PSF} , in units of the galaxies half-light radii. There is a correlation between the measured gradients $\nabla(B - I)_{Voronoi}$ and $r_{PSF}/r_{1/2}$: not surprisingly, the gradients become flatter with increasing FWHM of the PSF. To minimize this effect, at least in a statistical manner, we derived

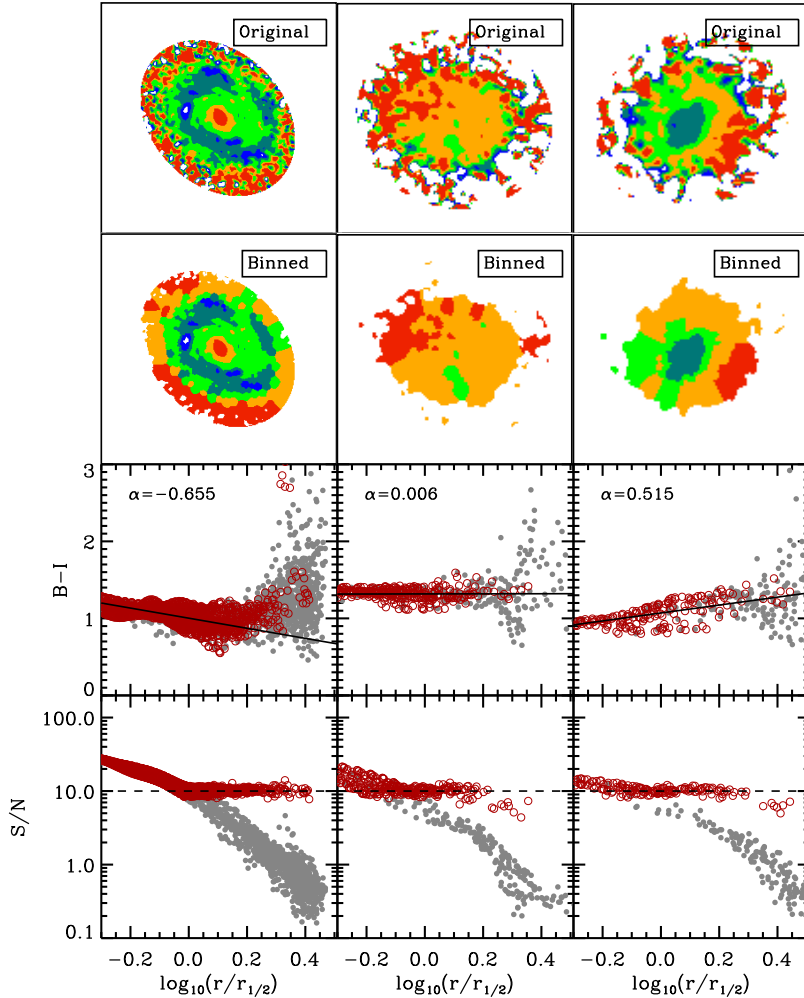


Figure 10. Examples of the Voronoi tessellated color maps for three of the ZENS galaxies. From left to right the figure shows a galaxy with negative color gradient (i.e., outer regions bluer than the nucleus), one with a flat profile and one with positive gradient (outskirts redder than the nucleus). The top panels show the original un-tessellated color maps; the seconds from the top show the Voronoi-tessellated maps. The next two rows are, respectively, the azimuthally-averaged color and signal-to-noise radial profiles. Gray symbols correspond to the profiles derived from the original color maps (one in 20 points plotted for clarity); red empty points are the values obtained from the tessellated color maps. The lines in the third row panels are the best-fit linear relations to the tessellated profiles; the dashed lines in the bottom panels show the target S/N used for the tessellation. Radii are normalized to the galaxy half-light radius.

an empirical correction function by fitting a linear relation to the $\nabla(B - I)$ vs. $r_{PSF}/r_{1/2}$ relation, which is shown with a dashed line in Figure 12. This empirical correction was then applied to all the Voronoi gradients.

Figures 13 and 14 show respectively the comparison between the corrected $\nabla(B - I)_{Voronoi}$ color gradients and the $(B - I)_{r_{1/2}, Voronoi}$ colors with the corresponding GIM2D measurements. For reference, we also show as black points the uncorrected Voronoi gradients in the last panel of Figure 13. Overall the two methods give qualitatively consistent results, particularly for the $(B - I)_{r_{1/2}}$ values. Concerning the color gradients, the above correction ameliorates the situation, but the Voronoi-based gradients tend to remain slightly shallower than the GIM2D-based gradients. To understand the origin of

such residual difference we searched for potential systematic biases with galaxy inclination, magnitude, minimum radius used in the fits, as well as size of the PSF.

There is indeed a bias with galaxy inclination: galaxies with $\epsilon > 0.6$ lie systematically below the identity line in the first panel of Figure 13, mostly as a consequence of projection effects. Along the semi-minor axis, where projection effects are strongest, for example, a given Voronoi cell integrates a larger range of physical radii, causing color information to be smeared out and color profiles to be slightly flattened at these high inclinations. The difference between the Voronoi and GIM2D profiles depends also on galaxy magnitude: the difference is larger for fainter ($I > 17.5$) galaxies, whose $\nabla(B - I)_{Voronoi}$ and $(B - I)_{r_{1/2}, Voronoi}$ are respectively flatter and ~ 0.1

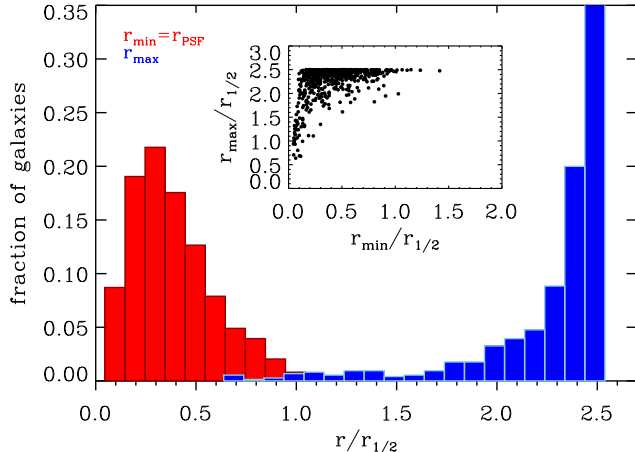


Figure 11. Distribution of minimum and maximum radii, in units of the global galaxy half-light radius, used to fit the azimuthally-averaged color profiles derived from the Voronoi-tessellated color maps. The minimum radius r_{PSF} is defined as the maximum between the B - and I -band PSF size. The inset shows the comparison between the minimum and maximum radius used for each galaxy.

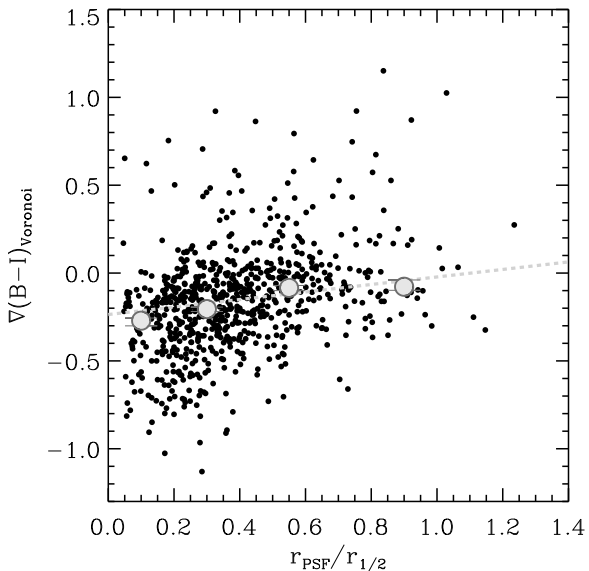


Figure 12. Color gradients $\nabla(B-I)_{Voronoi}$, i.e., derived by fitting the azimuthally-averaged color profiles obtained from the Voronoi tessellated color maps, as a function of the minimum radius used in the fits. Large grey points indicated the average color gradient in four bins of $r_{PSF}/r_{1/2}$; the dashed line is the result of the three-sigma-clipped linear least-squares fit used to statistically correct the “raw” $\nabla(B-I)_{Voronoi}$ values.

mag redder than the corresponding “GIM2D” measurements. This is most likely due to the contribution the night sky noise, which becomes more significant at the low surface brightness regime and longer wavelengths. After the application of the correction delineated above, no strong biases were however observed with the absolute or relative size of the PSF in either the Voronoi gradients or the Voronoi $(B-I)_{r_{1/2}}$ colors.

Given the above, and in order to recover measurements

of color gradients and colors at the half-light radius for galaxies without GIM2D fits (and minimize the bias in these measurements), we calculated the median residual differences between Voronoi and GIM2D color gradients and colors at the half-light radii, as a function of galaxy inclination and magnitude, and applied these additional correction functions to those galaxies for which no analytic color profile is available.

We finally highlight that, since (i) color gradients of highly-inclined (disk) galaxies as well as marginally resolved galaxies ($r_{1/2} < 1.5 \times PSF$) are, even when using GIM2D estimates, subject to larger errors, and (ii) high inclinations and small sizes may exacerbate physical biases introduced by absorption of light by interstellar dust, in our ZENS analyses, including those discussed in the following on this paper, we check that results hold when such galaxies are excluded from the sample. Similarly, we also check that results also hold when excluding galaxies with no GIM2D fits, i.e., galaxies for which we use the Voronoi gradients and colors (calibrated as above) in our analyses.

All measurements presented above will be used in future ZENS papers for detailed analyses of the stellar population and star formation properties of different galaxy populations as a function of different environmental parameters. In this paper we briefly investigate (1) global behavior of colors, color gradients and color dispersions at fixed Hubble type (from Paper II) and fixed stellar mass (Section 7; and (2) colors, color gradients and color dispersions of *satellite* galaxies in different environments (Section 8).

7. COLORS, COLOR GRADIENTS AND COLOR DISPERSIONS WITHIN GALAXIES: DEPENDENCE ON GALAXY STELLAR MASS AND HUBBLE TYPE

Figure 15 shows, from top to bottom, the median values of the $(B-I)_{r_{1/2}}$, $\nabla(B-I)$ and $\sigma(B-I)$ distributions as a function of galaxy stellar mass and at fixed Hubble type. We remind that we mainly use the GIM2D-based estimates for the spectra-photometric quantities, and in the following drop the subscript “GIM2D” for simplicity of notation. The colors at the half-light radii show the expected trends: they get redder with increasing galaxy mass and progressively earlier Hubble types. Also not surprising is the strong dependence of the color gradients on the morphological type: E/S0 galaxies show the flattest profiles, an indication that these galaxies have rather homogeneous stellar populations from their inner to their outer regions; late(r) morphological types show stronger color gradients, mostly as a consequence of redder bulges and segregation of star-forming regions in the outer disk regions.

Within each Hubble type, color gradients are however rather insensitive to stellar mass variations, and are typically $\nabla(B-I) \sim -0.3$ for intermediate- and late-type disks, and $\nabla(B-I) \sim -0.1$ for earlier morphological types. Also the color dispersion around the average color profile, $\sigma(B-I)$, is largely independent of galaxy mass for intermediate-type and late-type disk galaxies. We note however that, in the mass bins $M \gtrsim 10^{10.5} M_{\odot}$, most galaxies with such morphologies are central galaxies in our sample; when these are excluded from the analysis, there is a hint for a modest decline in the color dispersion with increasing galaxy stellar mass. The effect is

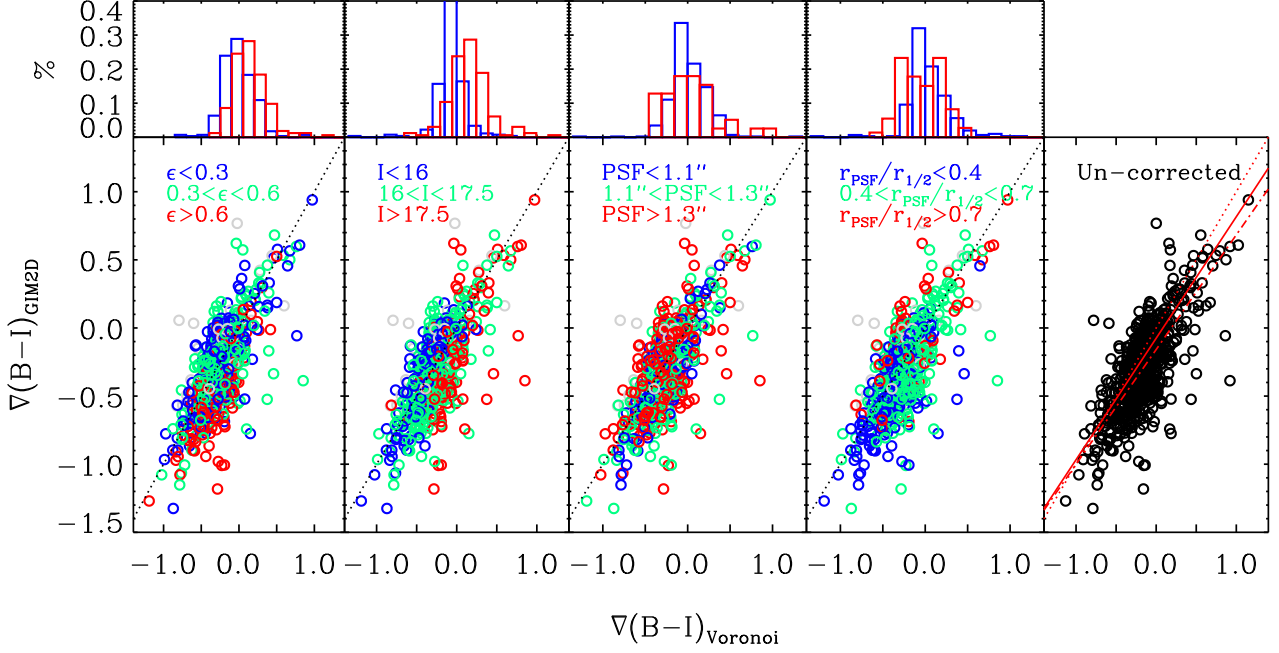


Figure 13. Comparison between color gradients $\nabla(B-I)_{Voronoi}$ derived from fits to the average color profiles obtained from the Voronoi tessellated color maps, and color gradients obtained from the analytical GIM2D Sérsic fits to the B - and I -band surface brightness profiles. ZENS galaxies are color-coded according to a number of observational diagnostics: from left to right, these are galaxy ellipticity, I -band magnitude, minimum radius used in the fits to the color profile, and the maximum size between the B - and I -band PSF. In the last panel the black points show the values of the Voronoi gradients before applying the empirical correction which takes into account the effect of masking the central r_{PSF} region. The histograms on top of each panel show the distributions of differences between Voronoi and GIM2D gradients in the lowest (blue) and highest (red) bin of the given parameters. Dotted lines indicate the identity line. In the right-most panel, solid and dashed-dotted lines are the best-fit to the corrected and uncorrected $\nabla(B-I)_{Voronoi}$ measurements. Grey symbols identify “troublesome” galaxies with possible bright star contamination to their photometry or whose fits to the color profiles are restricted within 1.3 half-light radii or less.

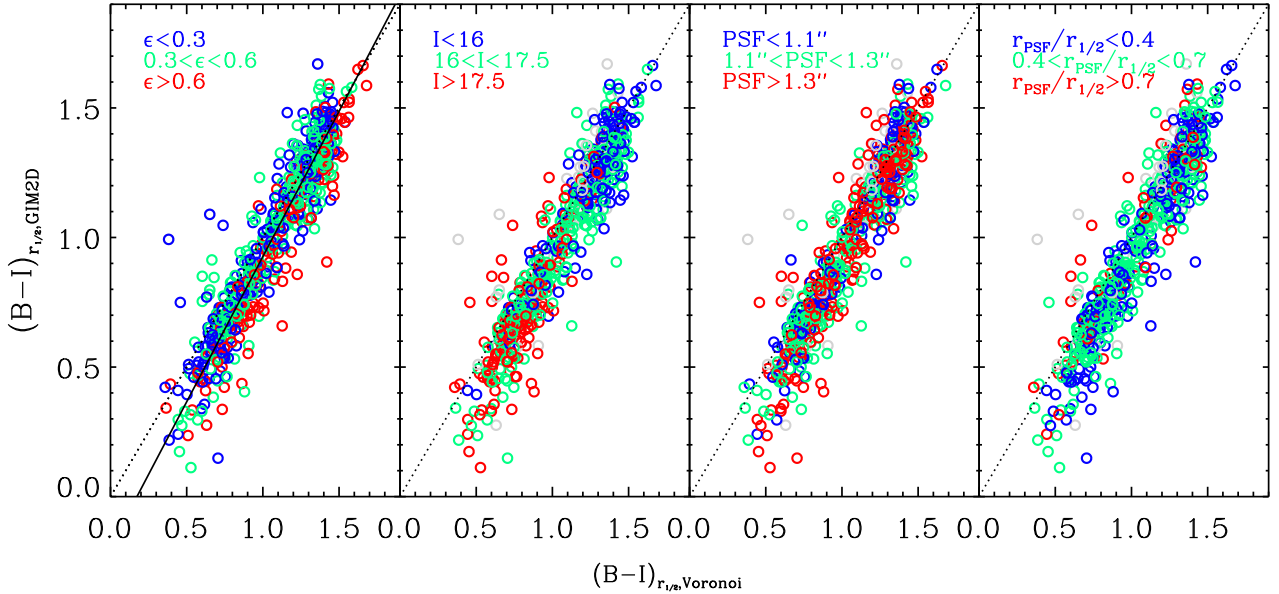


Figure 14. As in Figure 13, but for the $(B-I)_{r_{1/2}}$ measurements. The dotted and solid lines show the identity line and the fit to the points, respectively.

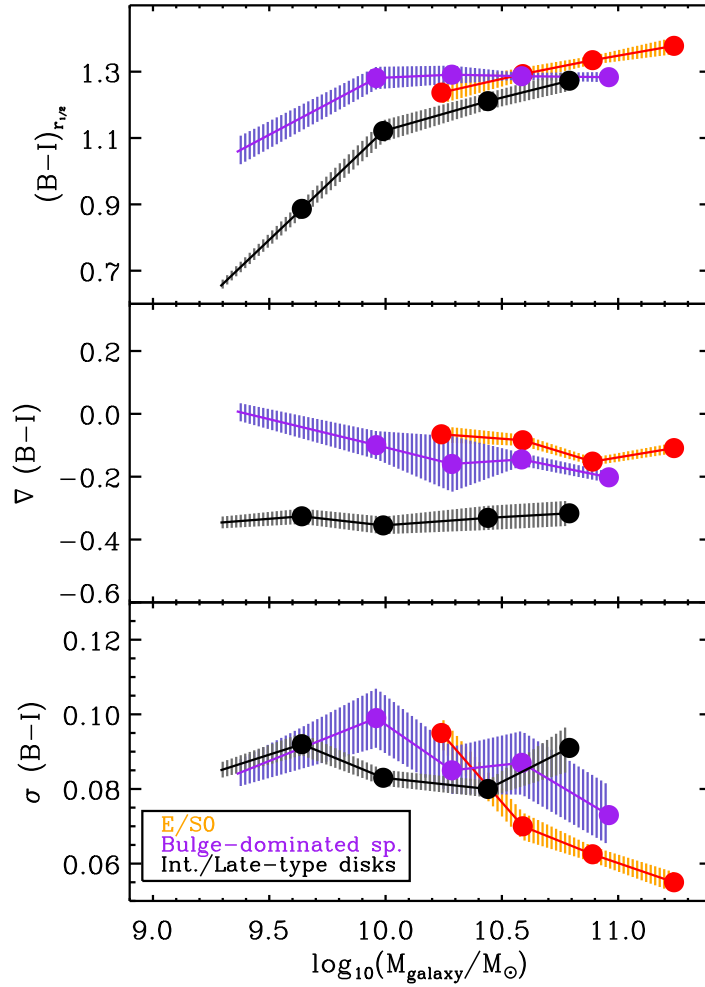


Figure 15. For the ZENS galaxies, from top to bottom, median colors at the half-light radii, color gradients, and rms scatter around the best-fit color profiles as a function of galaxy stellar mass. Colors correspond to the three morphological classes as identified in the legend (and defined in Paper II). The left-most filled symbol in each curve identifies the stellar mass completeness threshold for the given galaxy population. The shaded areas show the 1σ confidence levels.

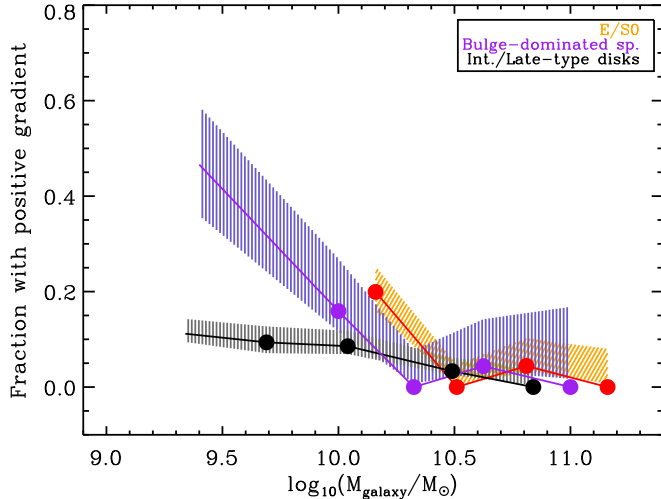


Figure 16. Fraction of galaxies with positive (“inverted”) color gradients, i.e., with blue nuclei and red outskirts, as function of galaxy stellar mass at fixed morphological type. Shaded areas show the 1σ confidence levels on the fractions, derived using the beta distribution quantile technique (see Cameron 2011). The fractions are corrected for 2dFGRS spectroscopic incompleteness. The left-most filled symbol in each curve identifies the stellar mass completeness threshold for the given galaxy population.

stronger at earlier morphological types: E/S0 galaxies show a net increase in color scatter around the average color gradient with decreasing galaxy stellar mass.

Also noticeable is that a non negligible fraction of galaxies have positive color gradients, i.e., bluer centers relative to redder outer regions. Specifically, we divide the sample into three bins of color gradients, i.e., $\nabla(B-I) < -0.1$ (negative color gradients), $-0.1 < \nabla(B-I) < 0.1$ (flat color gradients) and $\nabla(B-I) > 0.1$ (positive or “inverted” color gradients), respectively. Figure 16 shows the frequency of galaxies with positive gradient as a function of galaxy stellar mass, again at fixed morphological type as before. The fraction of galaxies with inverted color gradients increases with decreasing galaxy stellar mass: above $10^{10.5}M_{\odot}$ virtually no galaxies have inverted color gradients, while at $10^{9.5-10}M_{\odot}$, between 10% and 20% of galaxies have such inverted color profiles, with the higher fraction interestingly detected for earlier morphological types (in particular, bulge-dominated spirals, which are well sampled down to $\sim 10^{9.8}M_{\odot}$ in our sample).

We defer to a subsequent paper an in-depth investigation of these inverted-color-gradient galaxies, in particular in relation to internal color differences between satellite and central galaxies, and between merging/interacting galaxies and their non-interacting counterparts.

8. COLORS, COLOR GRADIENTS AND COLOR DISPERSION OF SATELLITE GALAXIES IN DIFFERENT ENVIRONMENTS

As a first utilization of our spectro-photometric measurements for the first-epoch ZENS galaxies, we investigate, for the population of *disk satellite galaxies only* (i.e., excluding from this analysis both galaxies classified as ellipticals in Paper II, as well as the central galaxies of the groups), how the colors, color gradients and color

dispersion around these gradients depend, at constant stellar mass, on our three fiducial environmental indicators: the total mass of the host group halo M_{GROUP} , the distance of the satellites from the centers of their host groups (R/R_{200}) and the large scale (over)density field δ_{LSS} . This analysis complements the discussion in Paper IV on the variation with the same environmental parameters of the relative fractions of spectral and morphological types in the satellites population. Likewise we refer to Paper V for a detailed comparison between the colors of the disk and bulge components, also separately for central and satellite galaxies at stellar masses $> M^{10.7}M_{\odot}$, where both these populations are well represented in the ZENS sample.

A first thing we note here is that satellites’ nuclear ($B-I$) colors, i.e. the colors measured from the PSF-corrected profiles at $0.1r_{1/2}$, are fairly insensitive to any of the environmental parameters: all galaxies are equally red at their center, with central colors ranging from ~ 1.2 to ~ 1.4 with increasing galaxy mass, but with variations which are smaller than ~ 0.05 magnitude in the different environments.

Also largely independent of environment are the ($B-I$) colors (both integrated and measured at $r_{1/2}$), the color gradients and color dispersions of “bulge-dominated” satellites, as illustrated in Figure 17. Specifically, this figure shows, from top to bottom, median values for ($B-I$) colors, color gradients $\nabla(B-I)$, and color dispersions $\sigma(B-I)$, as a function of galaxy stellar mass for the satellite galaxies. Red is used to show the ($B-I$) $_{r_{1/2}}$ colors, measured at the galaxy half-light radii, for the broad morphological bin of “bulge-dominated galaxies”; this broad bin includes disk galaxies that are classified as S0 or bulge-dominated spirals in Paper II (to which we refer for details on the ZENS morphological classification). For the broad bin of “disk-dominated galaxies”, which includes the two narrower morphological bins of intermediate-type and late-type disks defined in Paper II, we use blue symbols to show the ($B-I$) $_{r_{1/2}}$ colors at the half-light radii, and green symbols to show the integrated ($B-I$) colors, obtained from the Petrosian photometry discussed in Section 3.1 (see discussion below). All median values were calculated using a running box of width 0.4 dex and step 0.3 dex in stellar mass for the disk-dominated galaxies and, considering the smaller size of the sample, in two independent mass bins above and below $10^{10.6}M_{\odot}$ for the bulge-dominated galaxies. In all bins in each panel, the used galaxy samples are above the mass completeness limits of the relevant morphological types, apart from a very marginal incompleteness in the lowest mass bin for the “disk-dominated galaxies”, as the intermediate-type disks (which are summed together to the late-type disks to build this broader morphological late-type bin) are formally complete only above a slightly higher stellar mass bin (see Section 3.3). We checked however that this small effect does not impact our results (see discussion below).

In Figure 17, filled and empty symbols show respectively “dense” and “sparse” environments, i.e., from left to right, group masses M_{GROUP} above and below $10^{13.4}M_{\odot}$ (left panels), group-centric distances larger and smaller than $R = 0.6R_{200}$ (central panels), and LSS overdensities above and below $\log_{10}(1+\delta_{LSS}) = 0.65$, respec-

tively¹³.

In any environment, at the galaxy mass scales of our study, bulge-dominated satellites are redder (as expected), have shallower color gradients and similar color dispersions relative to disk-dominated satellites. The only marginal hint for an environmental effect on the bulge-dominated satellite population is possibly that their color gradients may be shallower in lower environmental density regions (i.e., lower mass groups, outskirts of the groups, and low LSS over densities) relative to similar galaxies in higher environmental densities (i.e., higher mass groups, inner group regions, and high LSS over densities). In our sample this qualitative trend is however weak, and we defer to the analysis of a larger sample for a statistically significant confirmation of it.

Of all environments, the least effective in inducing differences in satellites’ properties within the explored galaxy mass range is the large-scale overdensity field, as neither the global or local colors, the color gradients, or the color scatter around the gradients show any substantial difference with LSS over density, either in disk-dominated or in bulge-dominated satellites (apart from the marginal effect mentioned above for the gradients in the bulge-dominated population).

In contrast, the “local” environment of the host group has a larger impact on global and local colors of disk-dominated satellite galaxies. Particularly strong is the effect that we measure at low galaxy stellar masses, $\sim 10^{9.5} M_{\odot}$, for a reddening of ~ 0.2 magnitudes in both the colors at $r_{1/2}$ and the integrated colors, in the disk-dominated satellite population inhabiting the centers of galaxy groups ($R < 0.6R_{200}$), relative to similar satellites in the outer regions of the group potentials. Also evident in our data is the fact that, at larger galaxy stellar mass scales $\sim > 10^{10} M_{\odot}$, disk-dominated satellites in high-mass groups ($M > 10^{13.4} M_{\odot}$) and in the dense innermost group regions ($R < 0.6R_{200}$) have, at constant galaxy mass, shallower color gradients by ≈ -0.2 relative to less massive groups and to the outer group regions ($\nabla(B-I) \sim -0.2$ vs. $\nabla(B-I) \sim -0.4$, respectively). We checked that these trends are not driven by a change in the morphological mix between intermediate-type disks and late-type disks within the broad disk-dominated morphological bin. Note that, as discussed in Paper I, errors on the group mass estimates tend to dilute intrinsic trends with group mass; the detect trend with group mass could thus be possibly even stronger in reality.

At galaxy stellar masses $> 10^{10} M_{\odot}$, disk-dominated satellites show colors at the galaxy $r_{1/2}$ (blue data in the upper raw panels of Figure) that are redder by $\Delta(B-I)_{r_{1/2}} \simeq 0.1$ magnitudes in high-mass groups and in dense group cores, relative to similar satellites in less

massive groups and in the outer group regions. This “reddening” effect at the galaxy $r_{1/2}$ ’s disappears however in the integrated $(B-I)$ colors (obtained within the Petrosian aperture defined in Section 3.1; green data in the same panels). The median bulge-to-total ratios, integrated above $10^{10} M_{\odot}$ in the disk-dominated satellite samples at $R < 0.6R_{200}$ and $R > 0.6R_{200}$, respectively, are 0.32 and 0.28; the median integrated $(B-I)$ colors of, separately, the bulge and disk components of these two samples, are respectively 1.26 and 1.44 at $R < 0.6R_{200}$ and 1.23 and 1.48 at $R > 0.6R_{200}$. All these values are thus very consistent with each other, within the uncertainties, indicating that the effect is not explained either by bulge-to-total variations or by variations in bulge and/or disk colors between the samples that are being compared. As further discussed in Carollo et al. 2012b (Paper IX, in preparation), the median bulge half-light radii and disk scale lengths, are however respectively 1.2 kpc and 2.3 kpc within $0.6R_{200}$, and 1.4 kpc and 2.8 kpc in the outer group regions, indicating that, in particular, disks of $> 10^{10} M_{\odot}$ disk-dominated satellites in the inner cores of groups are $\approx 20\%$ smaller in size, and thus their bulges are more prominent, i.e., less “embedded within the disks”, than it is the case at large group-centric distances. The sum of the bulge contribution to the integrated colors may thus dilute the environmental effect with R_{200} that is marginally seen, also at these masses, in the colors measured at $r_{1/2}$. We defer a deeper investigation of the colors and sizes of bulge and disk components of ZENS galaxies to Rudick et al. 2012 (Paper V) and Carollo et al. 2012b.

In the following we focus our attention on the color reddening of low-mass, $10^{9.5} M_{\odot}$ disk-dominated satellites within $0.6R_{200}$ relative to similar galaxies at larger group-centric distances (a result which is seen using both the colors at $r_{1/2}$ and the integrated colors). We also further analyze the shallower color gradients of larger-mass, $> 10^{10} M_{\odot}$ disk-dominated satellites at small group-centric distances and high group masses relative to similar satellites in the complementary environmental bins. Specifically we investigate the implications of these results using stellar population synthesis models, semi-analytic models of galaxy formation, and the “continuity equation” approach of Peng et al. 2010, 2012. We note that we have not attempted any correction for intrinsic dust absorption within galaxies. In interpreting colors as stellar population (histories) effects, we will exclude ZENS galaxies which are mostly affected by internal reddening effects, i.e., galaxies which are strongly star-forming but have red colors (see Section 5.2).

8.1. *Interpreting with stellar population models the color and color gradient environmental differences of disk-dominated satellites*

Despite the well-known degeneracy of optical colors towards age/metallicity/dust and star formation histories, the color difference that we have observed in low-mass disk-dominated satellites as a function of group-centric distance contains information on the origin of such environmental effect. In particular, while dust and, to a lesser extent, metallicity, do no doubt play a role, the $(B-I)$ color is quite sensitive to stellar populations age variations in spiral galaxies (e.g. MacArthur et al. 2004;

¹³ Note that the δ_{LSS} analysis includes only groups with $M_{GROUP} < 10^{13.4} M_{\odot}$, to minimize the degeneracy between group mass and LSS density: as discussed in Paper I, while by definition massive groups are located in high δ_{LSS} regions, groups with masses $< 10^{13.4} M_{\odot}$ cover a large range of LSS density regimes, thus enabling the disentanglement of effects due to one or the other of these two environmental parameters. All ZENS groups were otherwise used in this study, to increase the statistics, including the groups defined as unrelaxed in Paper I (see also Section 2); we checked however that, with slightly larger error bars, consistent results hold when excluding the unrelaxed groups from the analysis.

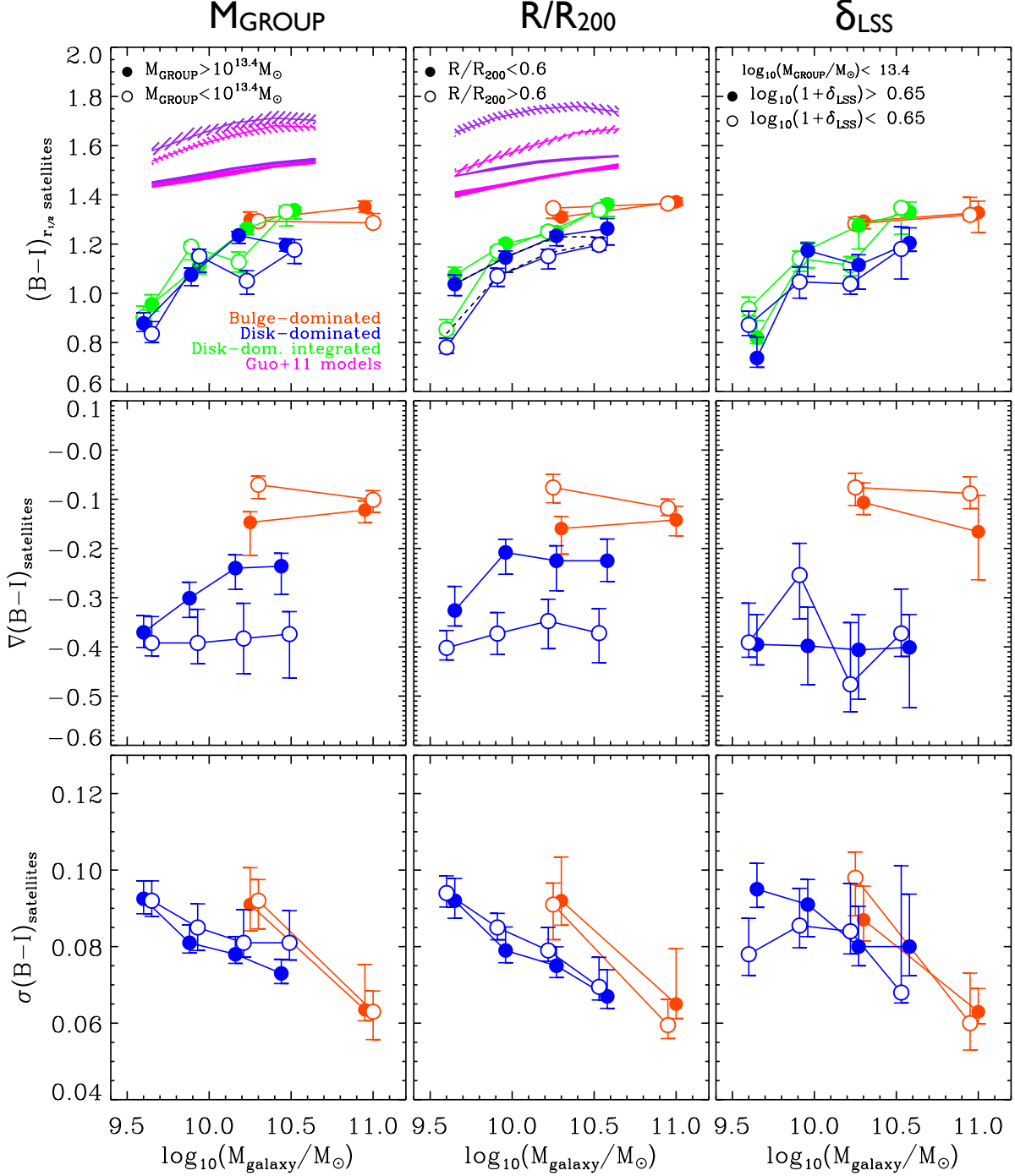


Figure 17. $(B - I)$ color (top panels), color gradients (central panels) and rms scatter around the best-fit color profiles (bottom panels) as a function of the galaxy mass for *disk satellite* galaxies in the ZENS groups. The top row shows in red and blue the results for the $(B - I)$ color computed at the galaxy half-light radius, i.e., the $(B - I)_{r_{1/2}}$ values; specifically, red indicates “bulge-dominated galaxies” (S0 plus bulge-dominated spirals), and blue “disk-dominated galaxies” (intermediate-type and late-type disks; see Paper II for details on the ZENS morphological classification). Overplotted in green in the top panels are the integrated $(B - I)$ colors for the disk-dominated galaxies (see text). From left to right, the galaxy sample is split in two environmental bins of, respectively group mass M_{GROUP} , group-centric distances (R/R_{200}) and LSS (δ_{LSS}) overdensity. Error bars correspond to the error on the median derived from the 16th and 84th percentiles. In magenta and purple we show the predictions of the Guo et al. (2011) semi-analytical model for the “sparser” and “denser” environment, respectively; in particular, dashed and solid curves are for models with and without dust reddening. Strongly star-forming galaxies with red colors (i.e., dust-reddened galaxies, see Section 5.2 and Figure 6) are excluded from this analysis; the effects of their inclusion is in any case minimal, as shown, as an example, by the dashed blue lines in the top middle panel (with effects of similar sizes in all other panels). Trends with the δ_{LSS} field are investigated restricting the sample to groups with $M_{GROUP} < 10^{13.4} M_{\odot}$, to avoid spurious effects with increasing δ_{LSS} due to the degeneracy between high δ_{LSS} values and high group mass.

Carollo et al. 2007). We thus assumed that the $(B - I)$ colors and color gradients that we have measured are mostly determined by the age of the underlying stellar populations. Despite the substantial uncertainty introduced in the derived age differences by this assumption, the differences provide a useful benchmark to rank stellar population properties between and within galaxies. In particular, since we will be comparing galaxy populations of similar Hubble type and stellar mass, the assumption that they have similar dust content and/or star formation histories is less uncomfortable than when comparing very different galaxy populations.

In constructing stellar population models for the comparison with the data, we constrained the stellar metallicity using the relation between galaxy stellar mass and stellar metallicity of Gallazzi et al. (2005), which, at the galaxy masses of our ZENS study, gives $Z_{\log M \in [9.5-10]} = 0.004 - 0.007$, $Z_{\log M \in [10.-10.5]} = 0.01 - 0.02$ and $Z_{\log M > 10.5} = 0.02 - 0.03$. We used BC03 templates with the above metallicities, an Chabrier (2003) initial mass function (IMF) and the same star-formation histories¹⁴ as in Table 2 to model the observed colors; we also assessed the impact of different galaxy template models by comparing the BC03-based results with the equivalent estimates based on the Charlot & Bruzual 2007 (CB07) libraries.

The observed color difference between $\sim 10^{9.5} M_{\odot}$ disk-dominated satellites within and outside $0.6R_{200}$, respectively, is consistent with a median ~ 2 Gyr age difference using either the CB07 and the BC03 templates, in the sense of “inner-group” disk-dominated satellites being older than “outer-group” disk-dominated satellites. As a consequence of the inclusion of the thermally pulsating AGB stars, the CB07 models reach redder colors at shorter times relative to the BC03 models, thus the spread around the median value is larger for the former (~ 2 Gyr) than for latter (~ 0.7 Gyr).

An alternative way to interpret the observed color difference between $\sim 10^{9.5} M_{\odot}$ disk-dominated satellites in the inner and outer group regions is in terms of a variation of the time scale over which star-formation occurs, i.e., in terms of τ variations within a the family of exponentially-declining star formation histories (after fixing the start of star formation activity to the same redshift, z_f , for all galaxies). Using the mass-metallicity relation above, z_f set to 10 Gyr ago and the BC03 models, the redder colors of these low-mass disk-dominated satellites in the inner-group regions correspond to ≈ 2 Gyr shorter τ values relative to similar satellites in the outer -group regions (i.e., $\tau_{R > 0.6R_{200}} \sim 6$ Gyr vs. $\tau_{R < 0.6R_{200}} \sim 3-4$ Gyr). We note that the CB07 models would give about twice as large τ differences between inner and outer groups regions.

With a typical galaxy crossing time within a ZENS group $t_{cr} = R_{200}/v \sim 10^9 \text{yr} \left(\frac{R_{200}}{\text{Mpc}} \right) \left(\frac{\sigma_{los}}{1000 \text{km s}^{-1}} \right)^{-1} \sim 1 - 3$ Gyr (where $R_{200} = \sqrt{3} \sigma_{los} / (10H(z))$, $H(z)$ is the expansion rate of the Universe at the median redshift $z = 0.055$ of the ZENS groups, and σ_{los} , i.e., the line-of-sight velocity dispersion of the group, is typically $\sim 200 - 400 \text{ km s}^{-1}$), the estimated τ differences between

low-mass disk-dominated satellites in the outer and inner group regions are comparable with the timescales of “migration” of these galaxies across their host groups. This interpretation thus supports a picture in which disk-dominated galaxies that plunge into galaxy groups, and become satellites within these potentials, see their star formation quenched, on timescales $\tau_{quench} \sim < 2$ Gyr, by physical processes which act on the satellites as they migrate towards the cores of the groups.

Following a similar approach, the color *gradients* that are observed *within* higher-mass, $> 10^{10} M_{\odot}$ disk-dominated satellite galaxies imply either (i) τ differences for the time scales of star formation through gas consumption in the inner vs. outer galactic regions of ~ 1.5 Gyr and ~ 3 Gyr, respectively, for the typical $\nabla(B - I) \simeq -0.2$ and $\nabla(B - I) \simeq -0.35$ gradients that are representative of the inner- and outer-group satellite populations at these galaxy mass scales; or, (ii) stellar age differences between the inner and outer *galactic* regions of ~ 3 Gyr and ~ 4 Gyr. The conclusion is therefore that the reddening of the half-light-radius color and the decrease in the strength of the color gradients probably both indicate that “satellite-quenching” preferentially acts on the outer parts of the disks, and occurs on an extended timescale of order ~ 2 Gyr as galaxies journey towards the group centers.

8.2. Comparisons with a state-of-the-art semi-analytic model

Semi-analytic models offer an alternative avenue to understand the color difference that we have observed between disk-dominated satellites in the cores and outskirts of groups. Several models have been developed; our scope here is however not to perform a complete comparison to identify the model which best fits the data, but, rather, to learn some lessons either from similarities or from differences between observations and a state-of-the-art semi-analytic model, which incorporates recipes to ameliorate known deficiencies in previous model generations. We thus focused our study on the Guo et al. (2011) (hereafter G11) model, based on the Millennium simulation (Springel et al. 2005). Since resolved color profiles are not available for the model, we used for the comparison with the ZENS galaxies their integrated $(B - I)$ colors (green data in Figure 17). Also, the default G11 colors are provided in the SDSS *ugriz* system; hence a conversion to $(B - I)$ was obtained using Table 2 of Blanton & Roweis (2007).

The G11 model was run on the Millennium simulation, on a box size of 685 Mpc, and has a resolution in galaxy stellar mass of a few $10^9 M_{\odot}$, well-suited for a comparison with the ZENS galaxies. G11 used a Chabrier IMF and included a treatment for dust to build the model galaxies. We created 10 random halo samples from all the haloes in the G11 volume, matching the number of groups and mass function of ZENS. From these halo samples we selected satellite galaxies, which were classified into two broad morphological types according to a stellar-mass bulge-to-total ratio threshold of $B/T=0.5$, i.e., $B/T \geq 0.5$ for bulge-dominated galaxies, and $B/T < 0.5$ for disk dominated galaxies. We note that a similar B/T numerical threshold is used to classify our ZENS sample in similar types, however in I -band light rather than stellar mass; thus, there might

¹⁴ Note that the reddest $(B - I)$ colors observed in Figure 17 are obtained only for models with $\tau < 7$ Gyr.

be a slight difference in morphological separation when comparing models and ZENS data, which we will keep in mind.

In virtually all semi-analytic computations, galaxies are found to be too red compared to real galaxies, a red-color excess that is interpreted as arising from the combination of a too fast gas consumption through star formation in the early phases of galaxy evolution relative to star formation histories of real galaxies, coupled with an excessive stripping of the hot gas when the galaxies are accreted onto a group halo (e.g. Weinmann et al. 2006; Font et al. 2008; Kimm et al. 2009; Fontanot et al. 2009). The G11 model includes an improved treatment of stripping of hot gas experienced by galaxies once they become satellites of larger haloes. As in other semi-analytic models, in G11 the hot-gas stripping happens after the galaxy enters the virial radius of the group. However, in contrast with earlier generations of models, in which the whole hot gas reservoir is instantaneously removed, in the G11 model only the gas outside a characteristic radius $R_{stripping}$ within the satellite’s own subhalo is removed (with $R_{stripping}$ set equal to the smallest between the tidal radius, in the group potential, of the dark matter component of the satellite’s subhalo, and the radius at which ram pressure stripping within the group potential equals the internal galaxy pressure). Satellites can thus retain a reservoir of hot gas in the G11 model, which keeps sustaining star formation activity after they enter the group virial radius. This helps reducing the (progressively larger at progressively lower masses) excess of quenched, red quiescent galaxies that is typically observed with respect to the observations in semi-analytic computations. The effect however is still present in the G11 model, as shown in the upper panels of Figure 17, where the model colors are shown in comparison with the ZENS data. Specifically, magenta and purple lines are the model median colors for disk-dominated satellites outside and within $0.6R_{200}$, respectively; dashed and solid curves describe models with and without dust reddening. The hatched lines are equivalent to the 1σ dispersion around the median, obtained from the 16th and 84th percentiles.

It is a success of the model, and a valuable insight for understanding our results, that the G11 model colors of disk-dominated satellites show similar environmental trends with group mass and group-centric distance than similar ZENS satellites. In the model, at constant galaxy mass, these satellites show colors that are almost independent of group mass; they become however substantially redder towards the group centers relative to the groups outskirts. Although not explicitly discussed in G11, this is likely due to a feature that seems to be common to several semi-analytic models (including some earlier versions of the G11 model, on which the latter is based; e.g., De Lucia & Blaizot 2007), as well as to dark-matter-only simulations (Gao et al. 2004): satellites that inhabit the group centers have entered the group virial radius at earlier times t_{infall} relative to satellites which are found in the outskirts of the groups. This “time delay” is typically of order $\Delta t_{infall} \sim 2 - 4 \text{ Gyr}$ (at least in the De Lucia & Blaizot 2007 model, as analyzed by De Lucia et al. 2012); this implies a relatively larger gas consumption and/or loss in the inner-group relative to the outer-group satellites. Similar trends for

satellites’ t_{infall} as a function of group-centric distance are also found in hydrodynamical simulations reproducing $z \sim 0$, $\sim 10^{13} M_{\odot}$ galaxy groups within a Λ CDM cosmology (Feldmann et al. 2011).

The G11 model furthermore also reproduces the fact that the color-reddening of disk-dominated satellites in inner- (relative to outer-) group regions is larger at lower (relative to higher) galaxy stellar masses. In the models this can be explained with a Δt_{infall} that decreases with increasing mass (from $\sim 4 \text{ Gyr}$ at $\sim 10^9 M_{\odot}$ to $\sim 2 \text{ Gyr}$ at $\sim 10^{11} M_{\odot}$ in the De Lucia et al. 2012 analysis), although a more efficient dynamical friction for high mass galaxies quickly moves these towards the inner group regions. In other words, low(er) mass galaxies are subject to the effects of ram pressure stripping for a factor > 2 longer time periods than the more massive satellites.

There are however also important discrepancies between the G11 model and the ZENS data, which are as illuminating as the successes highlighted above.

- First, as already stressed above, the G11 model predicts colors that are still significantly redder than real satellite galaxies at any galaxy mass of our study. In the models with no dust reddening, the discrepancy is of $\approx 0.2 - 0.3 \text{ mag}$, and grows to $\approx 0.5 \text{ mag}$ for the models with dust. A strictly quantitative comparison between data and models is difficult due to the slightly different morphological selection criteria, and the intervening conversion fractions for the colors discussed above. The size of the discrepancy is however substantial; furthermore, a similar discrepancy between model and SDSS data is already highlighted for the $u - i$ color in Figure 12 of Guo et al. (2011) (especially at stellar masses $\sim 10^{9.5} M_{\odot}$). We are thus confident of a genuine shift in color between the model and the data, in the direction of the model satellites being indeed redder than the ZENS satellites. This residual reddening of the G11 model relative to the ZENS data indicates that further revision of the model is required, most likely in the past star formation histories of present-day galaxies, so as to avoid gas over-consumption at early times while at the same time preventing excessive residual gas in galaxies at these mass scales at redshift $z = 0$.

- Furthermore, the model shows a stronger flattening of the color vs. galaxy mass relation than the real data: model colors remain essentially constant above $\sim 10^{10} M_{\odot}$, while ZENS satellites show a reddening of $\sim 0.15 \text{ mag}$ from $\sim 10^{10} M_{\odot}$ to $\sim 10^{10.7} M_{\odot}$. This indicates that the modification to the star formation rate histories in model galaxies needs to be increasingly larger with decreasing galaxy stellar mass.

- Finally, on quantitative ground, while the amount by which inner-group satellites are redder than outer-group satellites for low mass $\sim 10^{9.5} M_{\odot}$ satellites is similar (~ 0.2 magnitudes) between the observations and the model, at higher galaxy masses the latter shows a larger color difference between these two populations than the ZENS data. Possible interpretations of this discrepancy may be that, in the model, ram-pressure effects on massive galaxies, and/or their dynamical friction timescales, are over-estimated compared with ram pressure and time scales in the Universe. Alternatively, massive (disk-dominated) satellites in the real Universe may continue accreting gas also when close to the group

centers, in contrast with the model-assumption that no gas accretion on satellites takes place after they enter the virtualized group regions.

8.3. Interpreting environmental trends in colors and color gradients of disk-dominated satellites within a continuity-equation approach

The Peng et al. 2010 continuity approach to analyzing galaxy evolution has produced an impressively self-consistent picture of the overall evolution of the active and passive galaxy population since $z \sim 2$. Within the framework of this approach, Peng et al. 2012 studied a large sample of groups in the SDSS. While this methodology has been hitherto applied primarily to the integrated quantities of mass and star-formation rate, rather than morphology, it is nevertheless worth comparing the results of this section, and especially those concerning the overall $(B - I)$ colors of the galaxies (the upper panels in Figure 17), with those in Peng et al. 2012.

The independence of overall $(B - I)$ color for disk galaxies on group halo mass and the dependence on group-centric distance is certainly consistent with the finding by Peng et al. 2012 that the red fraction of satellites depends on local density within a group, but not on halo mass (at fixed density). The increasing impact of the group-centric radius environment with decreasing stellar mass of the galaxies is also consistent with the different characteristics of Peng et al.’s “mass-quenching” and “environment-quenching” processes. The rate of the former depends on the SFR, which is broadly proportional to the mass of star-forming galaxies, whereas the latter is, from the separability of the red fractions, independent of the stellar mass. Environment quenching thus dominates over mass-quenching at lower stellar masses, and especially so below $10^{10} M_{\odot}$.

The inclusion of morphological information in the continuity equation approach is planned (Peng et al. 2012, in preparation), and will enable a detailed comparison with the presented ZENS results.

9. SUMMARY AND CONCLUDING REMARKS

We have presented the photometric measurements for 769 galaxies in the first-epoch ZENS data. All measurements presented in this paper are included in the ZENS catalogue published in Paper I. Photometric galaxy parameters include total $(B - I)$ colors, color gradients, color dispersions, and galaxy stellar masses and star-formation rates, as well as bulge and disk $(B - I)$ colors and stellar masses, the latter based on the parametric bulge+disk decompositions in B and I presented in Paper II. Voronoi-tesselated two-dimensional $(B - I)$ color maps extending out to ~ 2 galaxy half-light radii were also obtained. ZENS galaxies were classified in the three spectral types of quiescent, moderately star forming, and strongly star forming systems, based on a spectral classification scheme using the combination of spectral absorption/emission features, broad-band (FUV) NUV-optical colors and SED fits to the available photometric data. The combination of multiple probes of star formation enables an efficient separation of red, quiescent systems from dust-reddened star forming galaxies; at $\sim 10^{10} M_{\odot}$, the latter are found to contribute up to 50% to the $(B - I)$ red-sequence.

In the ZENS sample as in others (see, e.g., Peletier et al. 1990; de Jong 1996; Jansen et al. 2000; Taylor et al. 2005; Gonzalez-Perez et al. 2011; Tortora et al. 2010), (i) average $(B - I)$ colors at the half-light radius steadily increase with galaxy stellar mass and towards earlier types; (ii) the intensity of $(B - I)$ color gradients correlates with morphological type, as defined using the structural parameters and morphological classification of Paper II: E/S0 galaxies have similarly shallow color gradients than bulge-dominated spiral galaxies [$\nabla(B - I) \sim -0.1 \div -0.2$]; such color gradients are substantially shallower than those of later-type, disk-dominated galaxies [$\nabla(B - I) \sim -0.3$]; (iii) most galaxies have negative color gradients (centers redder than outskirts); a non-negligible fraction of galaxies shows however flat or positive color gradients. At $M \sim 10^{10} M_{\odot}$, about 20% of galaxies of all morphological types have cores that are bluer than the outer galactic regions; the fraction of galaxies with inverted color gradients increases with decreasing galaxy stellar mass.

Focusing on *disk satellites* only, we have investigated, at fixed stellar mass and Hubble type, the dependence of $(B - I)$ colors (total and at the half-light radius), color gradients and color dispersion on all environmental parameters of Paper I, namely the mass of the host group M_{GROUP} , the distance from the group center in units of the group characteristic radius R_{200} , and the LSS overdensity field δ_{LSS} .

Bulge-dominated satellites have redder colors, shallower color gradients but similar color dispersion than disk-dominated satellites; albeit not in a statistically significant manner, our data seem to indicate that color gradients of bulge-dominated satellites may be shallower in regions of low environmental density – i.e., low mass groups, outer group regions and low LSS overdensities – compared to same Hubble type satellites in the corresponding denser environments. Apart from this possible exception, to be further verified on larger datasets, we find no evidence for an impact of the LSS density field on colors and color gradients of satellite galaxies of any Hubble type.

The group environment has instead a noticeable effect on both colors and color gradients of disk-dominated satellites. At galaxy masses $> 10^{10} M_{\odot}$, these satellites are found have shallower $(B - I)$ color gradients, by about -0.2 dex, in the inner $R < 0.6 R_{200}$ group regions relative to regions at larger group-centric distances, and at high group mass, above $M_{GROUP} = 10^{13.4} M_{\odot}$, relative to lower group masses; this is in agreement with the ~ 0.1 mag reddening with increasing halo mass of the colors profiles of $M < 10^{11} M_{\odot}$ satellites measured in SDSS (Weinmann et al. 2009). Furthermore, $> 10^{10} M_{\odot}$ disk-dominated satellites in our sample have ~ 0.1 magnitudes redder $(B - I)$ colors at the galaxy half-light radii in the inner group regions relative to similar satellites in the outer group regions, a color-reddening effect which is however not observed, at such high galaxy masses, in the integrated (rather than at $r_{1/2}$) colors. In contrast, both integrated and at half-light radius $(B - I)$ colors of lower-mass, $\sim 10^{9.5} M_{\odot}$ disk-dominated satellites are redder by ~ 0.2 magnitudes in the inner group regions relative to the group outskirts.

A simple stellar population analysis applied to the en-

environmental differences in $(B - I)$ colors and color gradients detected for disk-dominated ZENS satellites indicates star formation timescales $\tau \sim 2$ Gyr shorter, or ~ 2 Gyr older stellar populations, for low-mass disk-dominated satellites in the cores of groups relative to the group outskirts. These timescales are comparable with the timescales of satellite infall within the inner group regions, and are consistent with those derived in our Paper IV for the timescale of star formation quenching in satellites, τ_{quench} , as satellites migrate from the outskirts towards the cores of the groups. Similar timescales are found by other independent studies, which also estimate of order a couple of billion years for physical processes within the groups to act (e.g. Balogh et al. 2000; Weinmann et al. 2009; von der Linden et al. 2010; McGee et al. 2011; Wetzell et al. 2011; Feldmann et al. 2010, 2011).

Semi-analytical model predictions furthermore point at inner-group satellites to have an ~ 2 Gyr earlier infall time (and consequently earlier star formation quenching through loss of the hot gas reservoir and/or a similarly longer timescale for gas consumption) than outer-group satellites. A quantitative comparison shows however that even the Guo et al. (2011) model, which incorporates a progressive effect of ram pressure, still produces too red colors of satellite galaxies at the explored mass scales and Hubble types relative to the observations. A modification of the model is required so as to avoid excessive gas over-consumption at early times and, simultaneously, excessive residual gas in galaxies at redshift $z = 0$; most likely, both the star formation histories of galaxies and the feedback recipe need modifications. Such modifications need to be a function of galaxy stellar mass in order to reproduce the trends observed in the ZENS data.

The mass scales $< \sim 10^{10.5} M_{\odot}$ at which ZENS disk-dominated satellites most evidently show a reddening of their $(B - I)$ colors with decreasing distance from the group center are, at $z=0$, those shown by Peng et al. (2010) to be mostly affected by what they define as “environment-quenching”. Peng et al. (2012) furthermore showed that, at these galaxy mass scales, such environment-quenching is practically entirely due to environmental effects on galaxies as they become satellites of virialized groups: redder colors in high density environments are explained, following the continuity-equation approach of Peng et al. through quenching of star formation in the satellite galaxy population, not in central galaxies (“satellite-quenching”). The ZENS satellite analysis that we have presented adds further evidence to this scenario. In particular, our analysis supports that the “environment” affects galaxy evolution below a galaxy mass scale of $\approx 10^{10.5} M_{\odot}$ through physics which occurs within the group halos (van den Bosch et al. 2008; Weinmann et al. 2009; Guo et al. 2009; Peng et al. 2010). The fact that the strongest variation in the colors of low-mass disk-dominated satellites is observed as a function of the location within groups points to a physical mechanism for the “satellite-quenching” which either depends on the local density rather than the global halo potential, or affects the gas inflow, outflow and/or content of galaxies as they sink as satellites in the potentials of their host groups.

A.C., E.C., T.L. and C.R. acknowledge support from the Swiss National Science Foundation. This publication makes use of data from ESO Large Program 177.A-0680. This publication makes use of data products from the Two Micron All Sky Survey, which is a joint project of the University of Massachusetts and the Infrared Processing and Analysis Center/California Institute of Technology, funded by the National Aeronautics and Space Administration and the National Science Foundation. GALEX (*Galaxy Evolution Explorer*) is a NASA Small Explorer, launched in April 2003. We gratefully acknowledge NASA’s support for construction, operation, and science analysis for the GALEX mission.

REFERENCES

- Abazajian, K. N., Adelman-McCarthy, J. K., Agüeros, M. A., et al. 2009, *ApJS*, 182, 543
- Annibali, F., Bressan, A., Rampazzo, R., Zeilinger, W. W., Vega, O., & Panuzzo, P. 2010, *A&A*, 519, A40
- Baldry, I. K., Balogh, M. L., Bower, R. G., et al. 2006, *MNRAS*, 373, 469
- Baldwin, J. A., Phillips, M. M., & Terlevich, R. 1981, *PASP*, 93, 5
- Balogh, M. L., Navarro, J. F., & Morris, S. L. 2000, *ApJ*, 540, 113
- Balogh, M. L., Baldry, I. K., Nichol, R., Miller, C., Bower, R., & Glazebrook, K. 2004, *ApJ*, 615, L101
- Bamford, S. P., et al. 2009, *MNRAS*, 393, 1324
- Bell, E. F., McIntosh, D. H., Barden, M., et al. 2004, *ApJ*, 600, L11
- Bertin, E., & Arnouts, S. 1996, *A&AS*, 117, 393
- Biviano, A., Katgert, P., Thomas, T., & Adami, C. 2002, *A&A*, 387, 8
- Blanton, M. R., & Roweis, S. 2007, *AJ*, 133, 734
- Bolzonella, M., Kovač, K., Pozzetti, L., et al. 2010, *A&A*, 524, A76
- Brinchmann, J., Charlot, S., White, S. D. M., Tremonti, C., Kauffmann, G., Heckman, T., & Brinkmann, J. 2004, *MNRAS*, 351, 1151
- Bruzual, G., & Charlot, S. 2003, *MNRAS*, 344, 1000
- Bundy, K., Ellis, R. S., Conselice, C. J., et al. 2006, *ApJ*, 651, 120
- Bundy, K., Scarlata, C., Carollo, C. M., et al. 2010, *ApJ*, 719, 1969
- Caldwell, N. 1984, *PASP*, 96, 287
- Calzetti, D., Armus, L., Bohlin, R. C., Kinney, A. L., Koornneef, J., & Storchi-Bergmann, T. 2000, *ApJ*, 533, 682
- Cameron, E. 2011, *PASA*, 28, 128
- Cappellari, M., & Copin, Y. 2003, *MNRAS*, 342, 345
- Cardelli, J. A., Clayton, G. C., & Mathis, J. S. 1989, *ApJ*, 345, 245
- Carollo, C. M., Scarlata, C., Stiavelli, M., Wyse, R. F. G., & Mayer, L. 2007, *ApJ*, 658, 960
- Carollo, C. M., Cibinel, A., Lilly, S. J., et al. 2012 (Paper I), *ApJ*, submitted
- Carollo, C. M. et al. 2012b, in prep. (Paper IX)
- Cibinel, A., Carollo, C. M., Lilly, S. J., et al. 2012a (Paper III), *ApJ*, submitted
- Cibinel, A., Carollo, C. M. et al. 2012b, in prep. (Paper VIII)
- Cattaneo, A., Dekel, A., Devriendt, J., Guiderdoni, B., & Blaizot, J. 2006, *MNRAS*, 370, 1651
- Chabrier, G. 2003, *PASP*, 115, 763
- Colless, M., et al. 2001, *MNRAS*, 328, 1039
- Crain, R. A., Theuns, T., Dalla Vecchia, C., et al. 2009, *MNRAS*, 399, 1773
- Croton, D. J., Farrar, G. R., Norberg, P., et al. 2005, *MNRAS*, 356, 1155
- Daddi, E., Dickinson, M., Morrison, G., et al. 2007, *ApJ*, 670, 156
- Daigle, O., Carignan, C., Amram, P., et al. 2006, *MNRAS*, 367, 469
- Davoodi, P., Pozzi, F., Oliver, S., et al. 2006, *MNRAS*, 371, 1113
- de Jong, R. S. 1996, *A&A*, 313, 377
- Dekel, A., & Birnboim, Y. 2006, *MNRAS*, 368, 2
- De Lucia, G., & Blaizot, J. 2007, *MNRAS*, 375, 2
- De Lucia, G., Weinmann, S., Poggianti, B. M., Aragón-Salamanca, A., & Zaritsky, D. 2012, *MNRAS*, 3042

- Diehl, S., & Statler, T. S. 2006, *MNRAS*, 368, 497
- Dressler, A. 1980, *ApJ*, 236, 351
- Eke, V. R., Baugh, C. M., Cole, S., et al. 2004, *MNRAS*, 348, 866
- Feldmann, R., Carollo, C. M., Porciani, C., et al. 2006, *MNRAS*, 372, 565
- Feldmann, R., Carollo, C. M., Mayer, L., Renzini, A., Lake, G., Quinn, T., Stinson, G. S., & Yepes, G. 2010, *ApJ*, 709, 218
- Feldmann, R., Carollo, C. M., & Mayer, L. 2011, *ApJ*, 736, 88
- Ferreras, I., Lisker, T., Carollo, C. M., Lilly, S. J., & Mobasher, B. 2005, *ApJ*, 635, 243
- Font, A. S., Bower, R. G., McCarthy, I. G., et al. 2008, *MNRAS*, 389, 1619
- Fontanot, F., De Lucia, G., Monaco, P., Somerville, R. S., & Santini, P. 2009, *MNRAS*, 397, 1776
- Gallazzi, A., Charlot, S., Brinchmann, J., White, S. D. M., & Tremonti, C. A. 2005, *MNRAS*, 362, 41
- Gao, L., Springel, V., & White, S. D. M. 2005, *MNRAS*, 363, L66
- Gao, L., White, S. D. M., Jenkins, A., Stoehr, F., & Springel, V. 2004, *MNRAS*, 355, 819
- Gil de Paz, A., Boissier, S., Madore, B. F., et al. 2007, *ApJS*, 173, 185
- Gonzalez-Perez, V., Castander, F. J., & Kauffmann, G. 2011, *MNRAS*, 411, 1151
- Gunn, J. E., & Gott, J. R., III 1972, *ApJ*, 176, 1
- Guo, Y., McIntosh, D. H., Mo, H. J., et al. 2009, *MNRAS*, 398, 1129
- Guo, Q., White, S., Boylan-Kolchin, M., et al. 2011, *MNRAS*, 413, 101
- Hahn, O., Porciani, C., Carollo, C. M., & Dekel, A. 2007, *MNRAS*, 375, 489
- Hahn, O., Porciani, C., Dekel, A., & Carollo, C. M. 2009, *MNRAS*, 398, 1742
- Haines, C. P., Gargiulo, A., & Merluzzi, P. 2008, *MNRAS*, 385, 1201
- Heckman, T. M. 1980, *A&A*, 87, 152
- Ilbert, O., Salvato, M., Le Floch, E., et al. 2010, *ApJ*, 709, 644
- Jansen, R. A., Franx, M., Fabricant, D., & Caldwell, N. 2000, *ApJS*, 126, 271
- Karim, A., Schinnerer, E., Martínez-Sansigre, A., et al. 2011, *ApJ*, 730, 61
- Kauffmann, G., et al. 2003, *MNRAS*, 346, 1055
- Kauffmann, G., Heckman, T. M., White, S. D. M., et al. 2003, *MNRAS*, 341, 33
- Kawata, D., & Mulchaey, J. S. 2008, *ApJ*, 672, L103
- Khochfar, S., & Ostriker, J. P. 2008, *ApJ*, 680, 54
- Kimm, T., Somerville, R. S., Yi, S. K., et al. 2009, *MNRAS*, 394, 1131
- Kovač, K., Lilly, S. J., Knobel, C., et al. 2010, *ApJ*, 718, 86
- Kron, R. G. 1980, *ApJS*, 43, 305
- Larson, R. B., Tinsley, B. M., & Caldwell, C. N. 1980, *ApJ*, 237, 692
- Lemaux, B. C., Lubin, L. M., Shapley, A., Kocevski, D., Gal, R. R., & Squires, G. K. 2010, *ApJ*, 716, 970
- Lu, T., et al. 2012, in prep. (Paper IV)
- MacArthur, L. A., Courteau, S., Bell, E., & Holtzman, J. A. 2004, *ApJS*, 152, 175
- Macchetto, F., Pastoriza, M., Caon, N., Sparks, W. B., Giavalisco, M., Bender, R., & Capaccioli, M. 1996, *A&AS*, 120, 463
- Madgwick, D. S., Lahav, O., Baldry, I. K., et al. 2002, *MNRAS*, 333, 133
- Maller, A. H., Berlind, A. A., Blanton, M. R., & Hogg, D. W. 2009, *ApJ*, 691, 394
- Maulbetsch, C., Avila-Reese, V., Colín, P., et al. 2007, *ApJ*, 654, 53
- McGee, S. L., Balogh, M. L., Wilman, D. J., et al. 2011, *MNRAS*, 413, 996
- Noeske, K. G., Weiner, B. J., Faber, S. M., et al. 2007, *ApJ*, 660, L43
- Oemler, A., Jr. 1974, *ApJ*, 194, 1
- Oesch, P. A., Carollo, C. M., Feldmann, R., et al. 2010, *ApJ*, 714, L47
- Oke, J. B. 1974, *ApJS*, 27, 21
- Pannella, M., et al. 2009, *ApJ*, 698, L116
- Peng, Y.-j., Lilly, S. J., Kovač, K., et al. 2010, *ApJ*, 721, 193
- Peng, Y., Lilly, S. J., Renzini, A., & Carollo, M. 2012, arXiv:1106.2546
- Peletier, R. F., Davies, R. L., Illingworth, G. D., Davis, L. E., & Cawson, M. 1990, *AJ*, 100, 1091
- Phillips, M. M., Jenkins, C. R., Dopita, M. A., Sadler, E. M., & Binette, L. 1986, *AJ*, 91, 1062
- Pipino, A. et al. 2012, *ApJ*, in prep. (Paper VI)
- Pracy, M. B., Driver, S. P., De Propriis, R., Couch, W. J., & Nulsen, P. E. J. 2005, *MNRAS*, 364, 1147
- Pozzetti, L., Bolzonella, M., Lamareille, F., et al. 2007, *A&A*, 474, 443
- Pozzetti, L., Bolzonella, M., Zucca, E., et al. 2010, *A&A*, 523, A13
- Rudick, C. S. et al. et al. 2012a, in prep. (Paper V)
- Rudick, C. S. et al. 2012b, in prep. (Paper VII)
- Salim, S., Rich, R. M., Charlot, S., et al. 2007, *ApJS*, 173, 267
- Schlegel, D. J., Finkbeiner, D. P., & Davis, M. 1998, *ApJ*, 500, 525
- Sersic, J. L. 1968, Cordoba, Argentina: Observatorio Astronomico, 1968
- Sheth, R. K., & Tormen, G. 2004, *MNRAS*, 350, 1385
- Skibba, R. A. 2009, *MNRAS*, 392, 1467
- Skrutskie, M. F., Cutri, R. M., Stiening, R., et al. 2006, *AJ*, 131, 1163
- Springel, V., White, S. D. M., Jenkins, A., et al. 2005, *Nature*, 435, 629
- Taylor, V. A., Jansen, R. A., Windhorst, R. A., Odewahn, S. C., & Hibbard, J. E. 2005, *ApJ*, 630, 784
- Tremonti, C. A., et al. 2004, *ApJ*, 613, 898
- Tresse, L., Rola, C., Hammer, F., Stasińska, G., Le Fevre, O., Lilly, S. J., & Crampton, D. 1996, *MNRAS*, 281, 847
- Tortora, C., Napolitano, N. R., Cardone, V. F., Capaccioli, M., Jetzer, P., & Molinaro, R. 2010, *MNRAS*, 407, 144
- van den Bosch, F. C., Aquino, D., Yang, X., Mo, H. J., Pasquali, A., McIntosh, D. H., Weinmann, S. M., & Kang, X. 2008, *MNRAS*, 387, 79
- van der Wel, A. 2008, *ApJ*, 675, L13
- Veilleux, S., & Osterbrock, D. E. 1987, *ApJS*, 63, 295
- Veron, P., Goncalves, A. C., & Veron-Cetty, M.-P. 1997, *A&A*, 319, 52
- von der Linden, A., Wild, V., Kauffmann, G., White, S. D. M., & Weinmann, S. 2010, *MNRAS*, 404, 1231
- Weinmann, S. M., van den Bosch, F. C., Yang, X., & Mo, H. J. 2006b, *MNRAS*, 366, 2
- Weinmann, S. M., Kauffmann, G., van den Bosch, F. C., Pasquali, A., McIntosh, D. H., Mo, H., Yang, X., & Guo, Y. 2009, *MNRAS*, 394, 1213
- Wetzell, A. R., Tinker, J. L., & Conroy, C. 2011, arXiv:1107.531
- Williams, R. J., Quadri, R. F., Franx, M., van Dokkum, P., & Labbé, I. 2009, *ApJ*, 691, 1879
- Wyder, T. K., Treyer, M. A., Milliard, B., et al. 2005, *ApJ*, 619, L15
- Wuyts, S., Förster Schreiber, N. M., Lutz, D., et al. 2011, *ApJ*, 738, 106
- Yan, R., Newman, J. A., Faber, S. M., Konidaris, N., Koo, D., & Davis, M. 2006, *ApJ*, 648, 281
- York, D. G., Adelman, J., Anderson, J. E., Jr., et al. 2000, *AJ*, 120, 1579

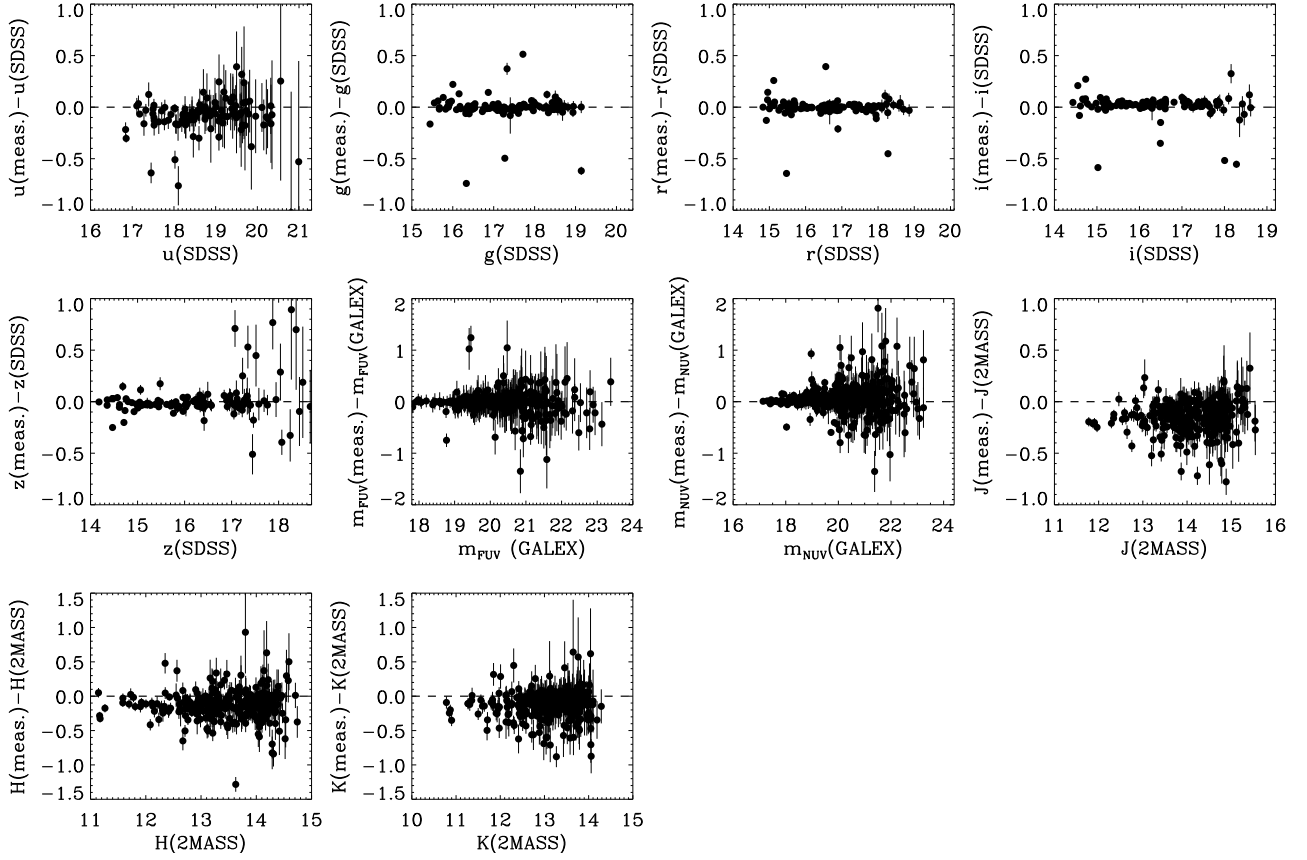


Figure A1. Comparison between the magnitudes that we measured on the public GALEX, SDSS and 2MASS images (indicated with “meas.”) and the magnitudes published by the survey teams (indicated with the names of the various surveys) for the first-epoch ZENS galaxies for which such data are available. The mag(GALEX) and mag(2MASS) data points refer to Kron (Kron 1980) magnitudes, and the mag(SDSS) data points to Petrosian fluxes; the latter are based on circular apertures. Our own measurements are performed on elliptical apertures with a semi-major axis equal to twice the largest between the WFI $B-$ and $I-$ band Petrosian radius.

APPENDIX

A. RELIABILITY OF THE SED FITS

In this Appendix we present the tests that we performed to assess the reliability of the photometric datasets which is used as input for the SED fits, and the robustness of the resulting mass estimates provided by ZEBRA+.

A.1. Impact of photometric errors on derived quantities

In Figure A1 we compare the magnitudes that we obtained by applying the aperture photometry described in Section 3.1 with the public measurements from the various surveys databases. The agreement is generally good, and deviations are in all cases smaller than 0.1 magnitudes. There are however some systematic effects: our SDSS and 2MASS magnitudes are slightly brighter than the published values. We have tested that this is partly due to our use of a larger aperture, indicating some flux losses in the published measurements. We also note that SDSS magnitudes are calculated using a circular aperture and hence part of the observed scatter stems from different aperture geometry. In fact, some of the most highly deviant points occur for highly inclined galaxies, for which the SDSS circular aperture was observed to miss a large fraction of the flux. Note also that a larger scatter in the magnitudes is observed for the GALEX-UV and SDSS u/z filters, which are noise-dominated.

Given the heterogeneous nature and origin of our photometry, the size of the PSF FWHM varies rather strongly across the probed wavelength range: from $\sim 5''$ for the GALEX ultra-violet data to sub-arcsecond resolution under the best observing condition for our own I -band imaging. In principle a matching of the images from the different surveys to a common PSF scale would be required to derive consistent color measurements. The use of a relatively large aperture ($2 \times R_p$) in the calculation of the magnitudes, however, effectively reduces PSF related biases. Indeed we tested on simulated data that degrading the quality of the images with the best PSF to the worst PSF increased rather than decreased the size of the errors on the derived quantities. Furthermore, we also checked on simulated images that using variable apertures in the different passbands does not improve the determination of stellar masses and other derived quantities, due to two effects, namely the increased noise in the degraded images, and a residual

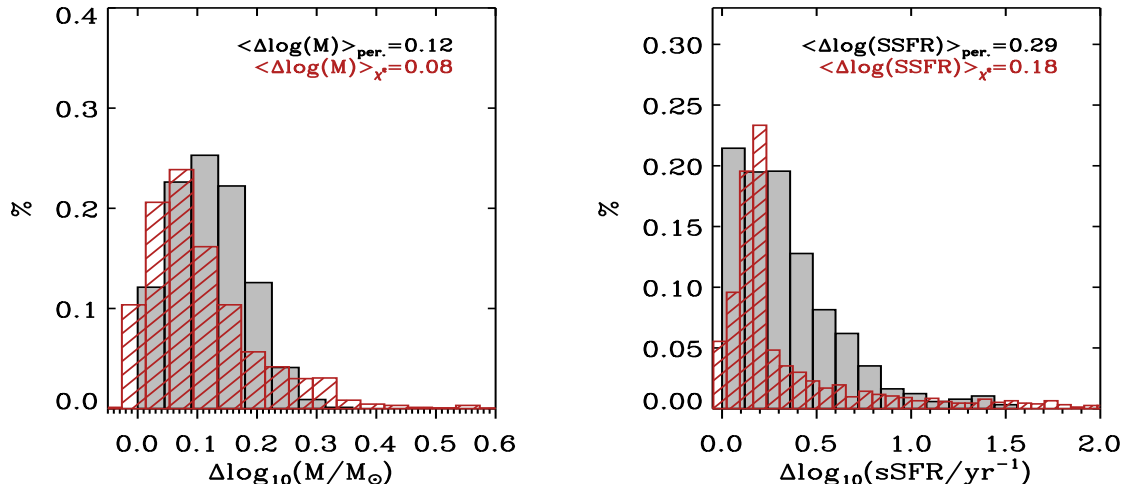


Figure A2. Distributions of the errors for the stellar masses and specific star-formation rates obtained from the ZEBRA+ SED fits. The gray histograms are for errors on the parameters calculated from the 16th and 84th percentiles of the likelihood distributions of the complete set of templates used in the fit. The red histograms show the typical uncertainties which are obtained by determining the values of the considered parameters which correspond to an increase of 50% in the value of χ^2 with respect to the minimum χ^2 of the best-fit templates. The corresponding median errors are indicated at the top of each panel.

contamination from nearby companions. As a final test for the reliability of our derived magnitudes, we smoothed the WFI I -band images – which have, on average, the best resolution – with a Gaussian kernel to reach a homogeneous 5 arcseconds PSF. We then re-measured on these smoothed images the flux inside the same Petrosian aperture used to derive the stellar masses in Section 3.1 and compared the resulting luminosities with the ones obtained from the unconvolved images. For about three quarters of the sample, the effect of PSF blurring causes flux variations which within the average photometric error in the I filter; furthermore, the difference remains within 0.1 magnitudes for about 90% of the sample. In the remaining few cases, differences of up to about 0.3 magnitudes were observed, both in the positive and in the negative direction, indicating that both flux losses and increased noise have an impact in this measurement. In these cases, the approach of deriving the galaxy fluxes on the original images guarantees higher quality measurements. We are therefore confident that the adopted scheme for measuring galaxy fluxes delivers stellar masses and related quantities which are robust to PSF variations across the spectral region of the used imaging dataset.

A.2. Errors on the ZEBRA+ stellar masses and (s)SFRs, and comparisons with the literature

To derive an uncertainty on the parameters obtained from the ZEBRA+ fits we utilized the likelihood and χ^2 distributions of the relevant quantities (masses, star-formation rates, specific star-formation rates, etc.) from the full set of the employed templates. Specifically, we derived the errors in two different ways, i.e., (i) using the 16th and 84th percentiles of the global likelihood distributions as our uncertainty measure, and (ii) deriving the values of the considered parameters which bracket an increase of 50% in χ^2 with respect to the χ^2 of the best fit template. We show the calculated errors in Figure A2 for galaxy masses and star-formation rates. The median error on the galaxy mass is ~ 0.1 dex and ~ 0.3 dex for the specific star-formation rates. As expected, (specific) star-formation rates are subject to larger uncertainties than the masses, hence our careful inspection of the spectral lines and color-color diagrams outlined in Section 5 to define the quiescent and star-forming populations substantially improves the purity of these samples relative to a simple cut in (SED-fit-based) sSFR.

As a further indication of the robustness of our stellar masses, we can use published measurements for a direct comparison. For about 30 galaxies in our sample, stellar masses are available from SDSS DR4 (Kauffmann et al. 2003b, derived from stellar absorption lines) and DR7 (Salim et al. 2007, calculated from fits to the photometry) analyses. In Figure A3 we show the comparison between these published masses and ours, estimated with ZEBRA+ SED fits. Figure A3 shows a good agreement between our masses and the values in the literature, with typical scatter of about 0.1 – 0.2 dex, consistent with the estimate calculated from the ZEBRA likelihoods. At a conservative 3σ level, the scatter in the stellar mass estimates is ~ 0.6 , i.e., remains within a factor of four in the worst cases.

A.3. Inclination effects

The derived photometric quantities need to be checked for a possible dependence on inclination (i.e., ellipticity). The light absorption by the interstellar dust is more severe at shorter wavelengths than in the red part of the spectrum and hence a poor treatment of the internal dust extinction could lead to fit highly inclined galaxies with preferentially older, less active – hence redder – templates than those used for face-on galaxies. Maller et al. (2009), for example, show a systematic offset in the estimates of stellar masses of for edge-on and face on galaxies in the SDSS analysis of Kauffmann et al. (2003b).

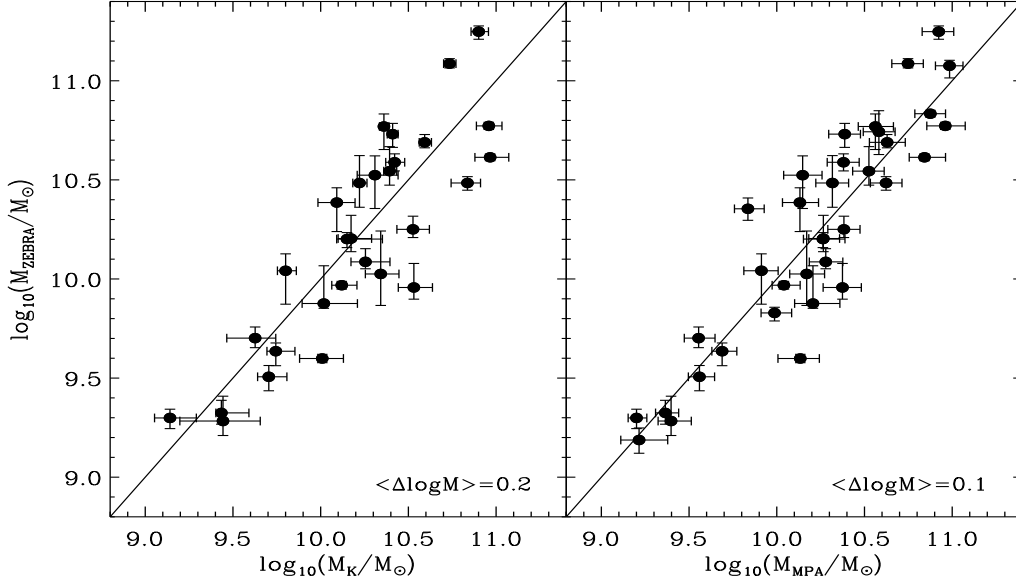


Figure A3. Comparison between stellar masses available in the literature and best fit masses measured by us with ZEBRA+ for a subsample of ZENS galaxies. The left panel shows the comparison with the SDSS DR4 (Kauffmann et al. 2003b) mass estimates based on the analysis of spectra absorption lines. The right panel shows the comparison with the DR7 masses based on photometric fits (see Salim et al. 2007). The median mass difference between our ZEBRA+ masses and the published ones is in both cases reported at the bottom-right corner of the panel.

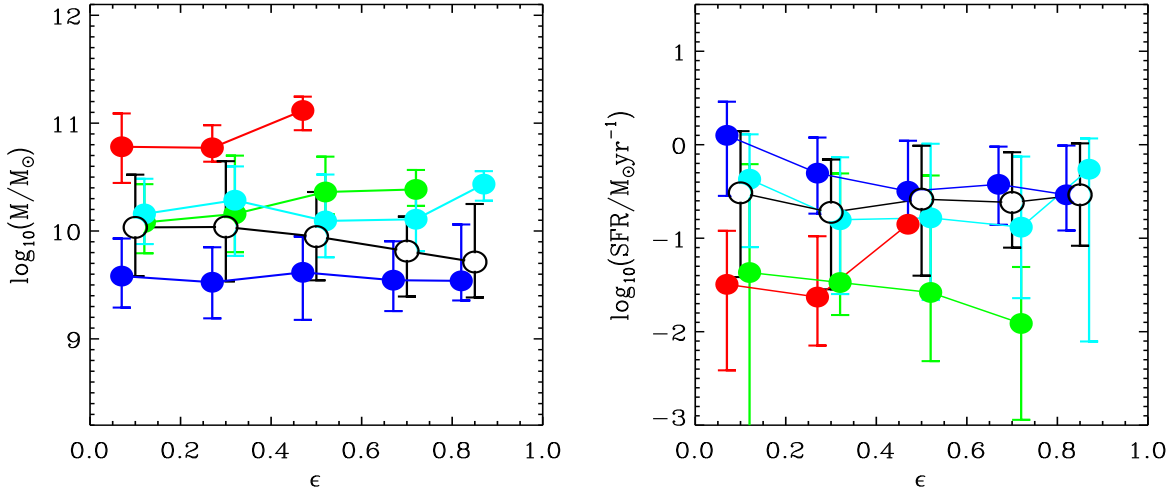


Figure A4. Median galaxy stellar mass and SFR as a function of ellipticity. Symbols with error bars are the median, in five ellipticity bins, for the global galaxy sample (black), and for morphologically-split samples of E/S0 galaxies (red), bulge-dominated spirals (green), intermediate-type disks (cyan) and late-type disks (blue). Error-bars show the 25th and 75th percentiles of the distributions. Ellipticities and morphological classes are taken from Paper II.

Using the structural parameters and morphological classifications presented in Paper II, we show in Figures A4 the ZEBRA+ galaxy masses and star-formation rates as a function of the measured galaxy ellipticity, both for the full sample of galaxies (black line in the figures), and also splitting the sample by morphological type (colored lines). Considering the global sample we find a slight decrease of stellar masses with ellipticity: looking at the morphological type separately, however, we see that the median mass is remarkably flat with increasing galaxy elongation and the aforementioned trend is simply a consequence of a changing morphological mix at a given axis ratio plus a different mass function of galaxy types. Regarding the SFR, there is a very modest decrease of the median SFR with ellipticity for late disk galaxies only, although the distributions for face-on and edge-on galaxies are statistically consistent. The other morphological types do not show any trends of masses and SFRs with ellipticity. We conclude that our estimates of (s)SFRs and stellar masses are not significantly biased with ellipticity.